Amplified role of potential HONO sources in O_3 formation in North China Plain during autumn haze aggravating processes

Jingwei Zhang[1][**], Chaofan Lian[2,3][**], Weigang Wang[2,3][*], Maofa Ge[2,3,7], Yitian Guo[1,4], Haiyan Ran[1,4], Yusheng Zhang[5], Feixue Zheng[5], Xiaolong Fan[5], Chao Yan[6], Kaspar R. Daellenbach[6], Yongchun Liu[5], Markku Kulmala[5,6], Junling An[1,4,7][*]

1. State Key Laboratory of Atmospheric Boundary Layer Physics and Atmospheric Chemistry (LAPC), Institute of Atmospheric Physics (IAP), Chinese Academy of Sciences, Beijing 100029, China

2. State Key Laboratory for Structural Chemistry of Unstable and Stable Species, Beijing National Laboratory for Molecular Sciences (BNLMS), CAS Research/Education Center for Excellence in Molecular Sciences, Institute of Chemistry, Chinese Academy of Sciences, Beijing 100190, China

3. School of Chemical Sciences, University of Chinese Academy of Sciences, Beijing 100049, China

4. College of Earth and Planetary Sciences, University of the Chinese Academy of Sciences, Beijing 100049, China

5. Aerosol and Haze Laboratory, Advanced Innovation Center for Soft Matter Science and Engineering, Beijing University of Chemical Technology, Beijing, 100029, China

6. Institute for Atmospheric and Earth System Research/Physics, Faculty of Science, P.O. Box 64, 00014 University of Helsinki, Helsinki, Finland

7. Center for Excellence in Urban Atmospheric Environment, Institute of Urban Environment, Chinese Academy of Sciences, Xiamen 361021, China

[*]Corresponding author: Weigang Wang (wangwg@iccas.ac.cn), Junling An (anjl@mail.iap.ac.cn)

[**]These authors contributed equally.

Abstract:

Co-occurrences of high concentrations of $PM_{2.5}$ and ozone (O_3) have been frequently observed in haze aggravating processes in the North China Plain (NCP) over the past few years. Higher O_3 concentrations in hazy days were supposed to be related to nitrous acid (HONO), but the key sources of HONO enhancing O_3 during haze aggravating processes remain unclear. We added six potential HONO sources, i.e., four ground-based (traffic, soil, and indoor emissions, and the NO_2 heterogeneous reaction on ground surface (Het_{ground})) sources, and two aerosol-related (the NO_2 heterogeneous reaction on aerosol surfaces ($Het_{aerosol}$) and nitrate photolysis ($Phot_{nitrate}$)) sources into the WRF-Chem model and designed 23 simulation scenarios

to explore the unclear key sources. The results indicate that ground-based HONO

sources producing HONO enhancements showed a rapid decrease with height, while

the NO+OH reaction and aerosol-related HONO sources decreased slowly with height.

$Phot_{nitrate}$ contributions to HONO concentrations enhanced with aggravated pollution

levels. The enhanced HONO due to $Phot_{nitrate}$ in hazy days was about ten times larger

than in clean days and $Phot_{nitrate}$ dominated daytime HONO sources (~30–70% when

the ratio of the photolysis frequency of nitrate ($J_{nitrate}$) to gas nitric acid (J_{HNO3}) equals

30) at higher layers (>800 m). Compared with that in clean days, the $Phot_{nitrate}$

contribution to the enhanced daily maximum 8-h averaged (DMA8) O_3 was increased

by over one magnitude during the haze aggravating process. $Phot_{nitrate}$ contributed

only ~5% of the surface HONO in daytime with a $J_{nitrate}/J_{HNO3}$ ratio of 30 but

contributed ~30–50% of the enhanced O_3 near the surface in NCP in hazy days.

Surface O_3 was dominated by volatile organic compounds-sensitive chemistry, while

O_3 at higher altitude (>800m) was dominated by NO_x-sensitive chemistry. $Phot_{nitrate}$

had a limited impact on nitrate concentrations (<15%) even with a $J_{nitrate}/J_{HNO3}$ ratio of

120. The above results suggest the potential but significant impact of $Phot_{nitrate}$ on O_3

formation, and that more comprehensive studies on $Phot_{nitrate}$ in the atmosphere are

still needed.

1. Introduction

Nitrous acid (HONO) is an important source of the hydroxyl radical (OH) through

2

its photolysis (R1), and contributes ~20–80% of the primary OH production (Alicke

et al., 2002; Hendrick et al., 2014; Kim et al., 2014).

$$HONO + hv \rightarrow NO + OH \quad (R1)$$
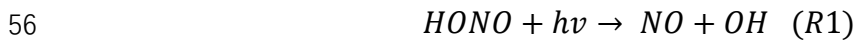
Although it has passed forty years since the first detection of HONO in the

atmosphere (Perner and Platt, 1979), the sources of HONO (especially daytime) and

the dynamic parameters of HONO formation mechanisms are still not well understood

(Ge et al., 2021). The current air quality models with the default gas-phase reaction

(the reverse reaction of R1) always severely underestimate HONO observations,

resulting in low atmospheric oxidation capacity and underestimation of secondary

pollutants like ozone (O_3) (Li et al., 2010, 2011; Sarwar et al., 2008; Zhang et al.,

2016, 2019a).

HONO sources can be generally classified into three categories, i.e., direct

emissions, homogeneous and heterogeneous reactions. Direction emissions are mainly

from traffic (Kramer et al., 2020; Kurtenbach et al., 2001; Liao et al., 2021), soil

(Kubota and Asami, 1985; Oswald et al., 2013; Wu et al., 2019; Xue et al., 2021),

biomass burning (Cui et al., 2021; Rondon and Sanhueza, 1989; Theys et al., 2020)

and indoor combustion processes (Klosterkother et al., 2021; Liu et al., 2019; Pitts et

al., 1985). The reaction of nitric oxide (NO) with OH (Pagsberg et al., 1997; Stuhl and

Niki, 1972) is usually thought as the dominant homogeneous reaction and is important

during daytime but could be neglected at night due to low OH concentrations, other

minor homogeneous HONO sources including nucleation of NO_2, H_2O, and NH_3

(Zhang and Tao, 2010), via the photolysis of ortho-nitrophenols (Bejan et al., 2006;

76   Chen et al., 2021; Lee et al., 2016), via the electronically excited NO_2 and H_2O

77   (Crowley and Carl, 1997; Dillon and Crowley, 2018; Li et al., 2008) and via

78      $HO_2 \cdot H_2O + NO_2$ reaction (Li et al., 2015; Li et al., 2014; Ye et al., 2015). The

79   heterogeneous reactions mainly include nitrogen dioxide (NO_2) hydrolysis and

80   reduction reactions on various humid surfaces (Finlayson-Pitts et al., 2003; Ge et al.,

81   2019; Gómez Alvarez et al., 2014; Ma et al., 2013; Marion et al., 2021; Sakamaki et

82   al., 1983; Tang et al., 2017; Yang et al., 2021b) and nitrate photolysis ($Phot_{nitrate}$)

83   (Romer et al., 2018; Ye et al., 2016a, b; Zhou et al., 2003), and are usually thought as

84   the main contributors to HONO concentrations in the atmosphere.

85   Among those potential HONO sources, the photolysis of nitrate to produce HONO

86   in the atmosphere has received extensive attention over the past several years, and the

87      $Phot_{nitrate}$ frequency ($J_{nitrate}$) is still argued (Gen et al.., 2022). In the laboratory studies,

88   some researchers (Bao et al., 2018; Ye et al., 2016a, 2017) showed that $Phot_{nitrate}$ was

89   an important HONO source, the measured $J_{nitrate}$ was 1–3 orders larger than the gas

90   nitric acid (HNO_3) photolysis frequency (J_{HNO3}) and could reach up to 10^{-4} s^{-1}, and a

91   number of substances including humic acid (Yang et al., 2018), sulfate (Bao et al.,

92   2020) and TiO_2 (Xu et al., 2021) might enhance the reaction significantly; while Shi et

93   al. (2021) found that the $J_{nitrate}/J_{HNO3}$ ratio was <10 when using suspended submicron

94   particulate sodium and ammonium nitrate rather than $PM_{2.5}$ samples. In the field

95   studies combining with model simulations, Kasibhatla et al. (2018) compared NO_x

96   observations in Cape Verde Atmospheric Observatory with GEOS-Chem (Goddard

97   Earth Observing System-Chemistry) model simulations and reported a $J_{nitrate}/J_{HNO3}$

98 ratio of 25–50, Romer et al. (2018) reported a $J_{nitrate}/J_{HNO3}$ ratio of < 30 based on

99 observations of NO_x (= NO + NO_2) and HNO_3 over the Yellow Sea and a box model

100 simulation, while larger $J_{nitrate}/J_{HNO3}$ ratios (e.g., 300) were inconsistent with the

101 observed NO_x to HNO_3 ratios. Adopting a $J_{nitrate}/J_{HNO3}$ ratio of ~120 could greatly

102 improve daytime surface HONO simulations (contributed ~30–40% of noontime

103 HONO) by using the Community Multiscale Air Quality model (CMAQ) in the Pearl

104 River Delta (Fu et al., 2019) or a box model in the Yangtze River Delta (Shi et al.,

105 2020), while a $J_{nitrate}/J_{HNO3}$ ratio of 30 produced negligible HONO in clean periods

106 (~2%) and slightly higher HONO in heavy haze periods (~8%) in the North China

107 Plain (NCP) by using a box model (Xue et al., 2020) and ~1% by using CMAQ in

108 urban Beijing (Zhang et al., 2021). Recently, Zheng et al. (2020) evaluated the effect

109 of three $J_{nitrate}/J_{HNO3}$ ratios (1, 10 and 100) on heterogeneous sulfate formation by

110 using CMAQ and large uncertainties of simulated sulfate concentrations were

111 reported. The mostly adopted $J_{nitrate}/J_{HNO3}$ ratios were 1–30 or 100–120 with large

112 uncertainties, so more efforts are needed to better understand the $Phot_{nitrate}$ impact on

113 atmospheric oxidation capacity and concentrations of HONO and other secondary

114 pollutants.

115 A number of potential HONO sources (e.g., direct emissions, NO_2 heterogeneous

116 reactions and $Phot_{nitrate}$) have been coupled into several air quality models (An et al.,

117 2013; Fu et al., 2019; Guo et al., 2020; Li et al., 2010, 2011; Sarwar et al., 2008; Tang

118 et al., 2015; Xu et al., 2006; Zhang et al., 2019a, 2019b, 2020a, 2021, 2022) to

119 improve HONO simulations. The improved HONO sources can produce more OH,

which is favorable for the formation of O_3 (Fu et al., 2019; Guo et al., 2020; Li et al., 2010; Xing et al., 2019; Zhang et al., 2016, 2019a, 2022). O_3 can directly damage plants and threaten human health (Avnery et al., 2011a, b; Feng et al., 2015, 2019, 2022; Mills et al., 2007, 2018; Richards et al., 1958; Selin et al., 2009; Wilkinson et al., 2012; Zhao et al., 2021), an increasing trend of O_3 concentrations in China has been widely reported in recent years (Chen et al., 2020a; Li et al., 2020; Lu et al., 2020; Ma et al., 2016; Maji and Namdeo, 2021), and made O_3 pollution be a severe concern. A co-occurrence of high $PM_{2.5}$ and O_3 concentrations has been frequently found in China over the past few years, researchers speculated the significant role of HONO in producing O_3 enhancements (Feng et al., 2021; Fu et al., 2019; Tie et al., 2019; Yang et al., 2021a). Nevertheless, the current knowledge on the HONO difference in O_3 formation during clean and hazy days is still unclear, especially the relative contribution of each potential HONO source to O_3 enhancements during haze aggravating processes with a co-occurrence of high $PM_{2.5}$ and O_3 concentrations.

In this study, time series of pollutants including HONO, O_3, and nitrate were collected in NCP in Oct.11–31 of 2018, in which high concentrations of $PM_{2.5}$ accompanying by high O_3 concentrations were found at least twice in haze events. The specific role of each of potential HONO sources in O_3 formation will be explored during these haze events by coupling these potential HONO sources into the Weather Research and Forecasting model with Chemistry (WRF-Chem). The relative contribution of each potential HONO source to surface-averaged and vertically-averaged concentrations of HONO and O_3 will be quantified and the

142   uncertainty in key potential HONO sources (e.g., $J_{nitrate}$) will be discussed, in order to

143   find the key HONO sources resulting in O_3 enhancements in NCP in different

144   pollution levels (especially during haze aggravating processes).

145   2.   Data and methods

146   2.1 Observed data

147   The field observation was carried out during October 11–31, 2018, and the

148   observation site was located in the west campus of Beijing University of Chemical

149   Technology (BUCT, 116°18'37'' E, 39°56'56'' N) in Beijing. BUCT is an urban site

150   close to the third ring road of Beijing, with large human activities, including vehicle

151   emissions. Instruments were set on the 5th floor of the main teaching building. HONO

152   was measured with a home-made water-based long-path absorption photometer (Chen

153   et al., 2020b). A dual-channel absorption system was deployed to subtract the

154   potential interferences, e.g., NO_2 hydrolysis. A set of on-line commercial analyzers

155   (Thermo 48i, 42i, 49i, 43i) was used for measurements of CO, NO_x, O_3, and SO_2. To

156   be specific, the 42i used molybdenum NO_2-to-NO converter, there would be a NO_2

157   overestimation for the conversion of HONO, HNO_3, or other NO_y. Considering the

158   relatively lower concentration compared with NO_2, the impact would be minor. The

159   chemical composition of $PM_{2.5}$ was analyzed with a Time-of-Flight Aerosol Chemical

160   Speciation Monitor (ToF-ACSM, Aerodyne), ToF-ACSM was developed via Fröhlich

161   et al. (2013) for Non-refractory $PM_{2.5}$ measurement. The detailed usage could be

162   found in Liu et al. (2020), where ionization efficiency calibration of nitrate was

163 performed using 300 nm dry NH$_4$NO$_3$ every month during the observation. An online

164 Single Photon Ionization Time-of-Flight Mass Spectrometer (SPI-ToF-MS, Hexin)

165 was used for the detection of a large variety of volatile organic compounds (VOCs)

166 (Gao et al., 2013). Surface observations of O$_3$, NO$_2$, PM$_{2.5}$ and PM$_{10}$ at 95 sites in

167 NCP were obtained from https://quotsoft.net/air/, issued by the China Ministry of

168 Ecology and Environment; surface meteorological observations at 284 sites in NCP

169 were taken from the National Climatic Data Center, China Meteorological

170 Administration (**Fig.1**).

171 The vertical HONO observations were not available during the Oct.11–31 of 2018

172 at the BUCT site, we used the observed vertical HONO concentrations from Meng et

173 al. (2020) in urban Beijing in December of 2016 to evaluate our simulation of vertical

174 HONO concentrations, which were also used by Zhang et al. (2021) in their CMAQ

175 evaluation.

176

177 **2.2 Model description**

178 The improved WRF-Chem (version 3.7.1), which contained six potential HONO

179 sources, i.e., traffic (E$_{traffic}$), soil (E$_{soil}$), and indoor (E$_{indoor}$) emissions, Phot$_{nitrate}$ in the

180 atmosphere, and NO$_2$ heterogeneous reactions on aerosol (Het$_{aerosol}$) and ground

181 (Het$_{ground}$) surfaces (Zhang et al., 2019a), was used in this study. Phot$_{nitrate}$ was newly

182 added in WRF-Chem (R2) following the work of Fu et al. (2019), Ye et al. (2017),

183 and Zhou et al. (2003):

184 $$pNO_3 + hv \rightarrow 0.67HONO + 0.33NO_2 \quad (R2)$$
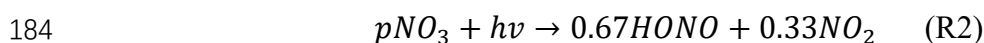
185   For Het$_{aerosol}$ and Het$_{ground}$, laboratory studies suggest that these heterogeneous

186   reactions of NO$_2$ to HONO are first order in NO$_2$ (Aumont et al., 2003;

187   Finlayson-Pitts et al., 2003; Saliba et al., 2000):

188     $$NO_2 \rightarrow HONO \quad k_a \quad \text{(R3)}$$

189     $$NO_2 \rightarrow HONO \quad k_g \quad \text{(R4)}$$

190   The first-order rate constants for aerosol (k_a) and ground (k_g) surface reactions

191   are calculated below:

192     $$k_a = \frac{1}{4} \times v_{NO_2} \times \left(\frac{S}{V}\right) \times \gamma \quad \text{(E1)}$$

193     $$k_g = \frac{f \times v_d}{H} \quad \text{(E2)}$$

194   where v_{NO_2} is the mean molecular speed of NO$_2$, $\frac{S}{V}$ is the surface to volume ratio for

195   aerosols, γ is the reactive uptake coefficient of aerosols, f is the proportion of

196   deposited NO$_2$ reaching the surface in participating HONO formation, v_d is the dry

197   deposition velocity of NO$_2$, and H is the first model layer height above the ground

198   (~35 m). It should be noted that not 100% (50% is commonly accepted) of the

199   participated NO$_2$ could be converted to HONO in R3 and R4, so k_a and k_g were

200   multiplied by 0.5 in the final calculation of HONO heterogeneous formation via NO$_2$.

201   The two factors γ and f were improved from previous studies (Li et al., 2010; Liu

202   et al., 2014; Zhang et al., 2019a) and calculated by:

203     $$\gamma = 5 \times 10^{-6} \times \left(1 + \frac{SR}{\alpha}\right) \quad \text{(E3)}$$

204     $$f = 0.08 \times \left(1 + \frac{SR}{\alpha}\right) \quad \text{(E4)}$$

205   where SR denotes solar radiation (W m^{-2}), α is an adjusted parameter and set as 100

206   (W m^{-2}), thus γ and f became continuous functions during the whole day (γ and f

207   enhanced by ten times and reached 5×10^{-5} and 0.8 when SR reached 900 W m^{-2} at

208   noontime, respectively).

209   The physical and chemical schemes used in this study are given in **Table 1**. Two

210   domains were adopted, domain one contains 82×64 grid cells with a horizontal

211   resolution of 81 km, domain two contains 51×51 grid cells with a horizontal

212   resolution of 27 km (**Fig.1**), both with 17 vertical layers encompassing from the

213   surface to 100 hPa. The observational sites are shown in the right panel of **Fig.1**,

214   including one HONO observation site (the orange dot in urban Beijing), 95

215   observation sites of PM$_{2.5}$, NO$_2$ and O$_3$ (pink dots) and 284 meteorological monitoring

216   sites (black dots).
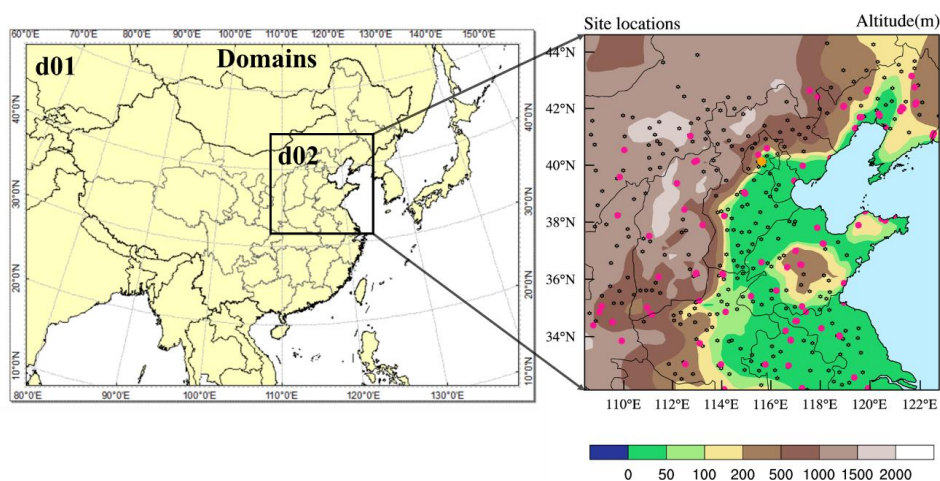
217

218   **Figure 1** Domains of WRF-Chem used in this study (left panel), and the locations of one HONO

219   observation site (the orange dot in urban Beijing), 95 environmental monitoring (PM$_{2.5}$, NO$_2$ and

220   O$_3$) sites (deep pink dots), and 284 meteorological observation sites (black dots) in domain 2 (right

221   panel).

222

223   The anthropogenic emissions in East Asia in 2010 were taken from the MIX

224   emission inventory (Li et al., 2017) (http://www.meicmodel.org/), including both

225   gaseous and aerosol species, i.e., SO_2, NO_x, CO, VOCs, NH_3, PM_{10}, $PM_{2.5}$, BC, OC

226   and CO_2, and were provided monthly by five sectors (power, industry, residential,

227   transportation, and agriculture) at a resolution of 0.25˚ × 0.25˚. VOC emissions were

228   speciated into model-ready inputs according to the MOZART chemical mechanism to

229   build the WRF-Chem emission files. The anthropogenic emissions in China were

230   replaced by employing the MEIC 2016 (the Multi-resolution Emission Inventory for

231   China) developed by Tsinghua University. The NH_3 emissions in China were from

232   Dong et al. (2010), biomass burning emissions were from Huang et al. (2012) and

233   biogenic emissions were calculated using the Model of Emissions of Gases and

234   Aerosols from Nature (MEGAN) (Guenther et al., 2012). Due to the sharp reduction

235   of anthropogenic emissions in recent years, the default emission inventory was

236   systematically overestimated in autumn of 2018, especially for SO_2 and $PM_{2.5}$

237   concentrations. Based on the comparison of simulations and observations (the urban

238   Beijing site plus other 95 pollutant monitoring sites in NCP), we cut off 80% of SO_2

239   emissions, 50% of NH_3 emissions, 30% of toluene emissions, and 50% of $PM_{2.5}$ and

240   PM_{10} emissions. The cut-off emissions are largely close to the emission reductions in

241   east China during 2013 to 2017 (Zhang and Geng, 2019). The revised emissions

242   significantly improved regional $PM_{2.5}$ simulations in NCP **(Fig.S1)**, and the

243   simulations of gases and $PM_{2.5}$ in urban Beijing **(Fig.S2)**.

244   The National Centers for Environmental Prediction (NCEP) 1° × 1° final

245   reanalysis data (FNL) (https://rda.ucar.edu/datasets/ds083.2/) were used in this study

246 to obtain the meteorological initial and boundary conditions every 6 h. The global

247 simulations of MOZART-4 (https://www.acom.ucar.edu/wrf-chem/mozart.shtml)

248 were used as the chemical initial and boundary conditions (every 6 h).

249

250 **Table1** Physical and chemical options in WRF-Chem used in this study

Options	WRF-Chem
Advection scheme	Runge-Kutta 3rd order
Boundary layer scheme	YSU
Cloud microphysics	Lin et al. (1983)
Cumulus parameterization	New Grell scheme
Land-surface model	Noah
Long-wave radiation	RRTM
Short-wave radiation	Goddard
Surface layer	Revised MM5 Monin-Obukhov scheme
Aerosol option	MOSAIC (Zaveri et al., 2008)
Chemistry option	Updated MOZART mechanism (Emmons et al., 2010)
Photolysis scheme	F-TUV

251

252 Totally 23 simulation scenarios were performed in this study (**Table 2**), in which

253 the base case only considered the default homogeneous reaction (OH + NO $\rightarrow$

254 HONO), case 6S contained six potential HONO sources while case A, B, C, D, E and

255 F contained each of the six potential HONO sources, respectively. Other 15 cases

256 (A_double, A_half, …, Nit_120, D_NO$_2$ and D_HONO) were used to evaluate the

257 uncertainties of the six potential HONO sources (**Table 2**). All of the cases were

258 simulated with a spin-up of 7 days. $J_{nitrate}$ and J_{HNO3} denote the photolysis frequency of

259 nitrate and gas nitric acid in the atmosphere, respectively. The enhancement factor for

260 F_double was 1.25 rather than 2.0 to avoid the production rate of HONO from NO$_2$

261 reaching the surface exceeding 100%. The 0.33NO$_2$ in D_NO$_2$ or 0.67HONO in

262 D_HONO referred to the assumed Phot$_{nitrate}$ products in R2.

263

Table 2. Simulation scenarios designed in this study.

Case	HONO sources
Base	Default (OH + NO $\rightarrow$ HONO)
6S	Default + $E_{traffic}$ + E_{soil} + E_{indoor} + Phot$_{nitrate}$ ($J_{nitrate}/J_{HNO3}$ = 30) + Het$_{aerosol}$ + Het$_{ground}$
A	Default + $E_{traffic}$
B	Default + E_{soil}
C	Default + E_{indoor}
D	Default + Phot$_{nitrate}$ ($J_{nitrate}/J_{HNO3}$ = 30)
E	Default + Het$_{aerosol}$
F	Default + Het$_{ground}$
A_double	Default + 2×$E_{traffic}$
A_half	Default + 0.5×$E_{traffic}$
B_double	Default + 2×E_{soil}
B_half	Default + 0.5×E_{soil}
C_double	Default + 2×E_{indoor}
C_half	Default + 0.5×E_{indoor}
E_double	Default + Het$_{aerosol}$ (2×γ)
E_half	Default + Het$_{aerosol}$ (0.5×γ)
F_double	Default + Het$_{ground}$ (1.25×f)
F_half	Default + Het$_{ground}$ (0.5×f)
Nit_1	Default + Phot$_{nitrate}$ ($J_{nitrate}/J_{HNO3}$ =1)
Nit_7	Default + Phot$_{nitrate}$ ($J_{nitrate}/J_{HNO3}$ = 7)
Nit_120	Default + Phot$_{nitrate}$ ($J_{nitrate}/J_{HNO3}$ = 120)
D_NO$_2$	Only 0.33NO$_2$ produced in Phot$_{nitrate}$ for case D
D_HONO	Only 0.67HONO produced in Phot$_{nitrate}$ for case D

265 **3.Results**

266 **3.1 Comparison of simulations and observations**

267 **3.1.1 Meteorological factors**

268   The statistical metrics of simulated meteorological parameters at 284 sites in NCP

269 including air temperature (T), relative humidity (RH) and wind speed (WS) were

270 comparable with the previous modelling results of other researchers (**Table 3**). The

271 simulated wind direction (WD) bias within 45° accounted for ~56%, and the bias

272 within 90° accounted for ~80%, suggesting that the simulated WD captured the main

273 observed WD.

274

Table 3. Performance metrics (index of agreement (IOA), RMSE (root-mean-square error) and MB (mean bias)) of WRF-Chem simulated air temperature, relative humidity, wind speed and direction at 284 meteorological sites in the North China Plain during Oct. 11–31 of 2018. The definitions of the metrics used in this study are given in **Text S1**.

	IOA	RMSE	MB	Reference
T (℃)	**0.97**	**1.4**	**-1.1**	**This work**
	0.90	2.5	0.2	(Wang et al., 2014)
	0.90	/	-0.9	(Wang et al., 2010)
	0.88	/	0.5	(Li et al., 2012)
	/	3.1	0.8	(Zhang et al., 2012)
RH (%)	**0.90**	**9.0**	**-7.1**	**This work**
	0.78	16.3	-5.5	(Wang et al., 2014)
	0.78	/	-1.3	(Wang et al., 2010)
	0.86	/	-1.1	(Li et al., 2012)
	/	17.4	-5.7	(Zhang et al., 2012)
WS (m s^{-1})	**0.48**	**1.4**	**1.3**	**This work**
	0.56	2.5	1.6	(Wang et al., 2014)
	0.65	2.1	0.9	(Wang et al., 2010)
	0.62	1.5	0.6	(Li et al., 2012)
	/	2.2	1.1	(Zhang et al., 2012)
WD Bias	*0-45°*	*45-90°*	*>90°*	
Count	*75701*	*21500*	*28075*	*135276(Total)*
Percentage	**55.96%**	**23.29%**	**20.75%**	

3.1.2 Pollutant concentrations at the BUCT site

Time series of the observational data at the BUCT site are shown in **Fig.2**, the gray shaded periods stand for three haze aggravating processes, while the cyan shaded period denotes typical clean days, respectively. The hourly largest observations of O_3 (~50–75 ppb) and $PM_{2.5}$ (~100–200 μg/m^3) were both relatively higher in hazy days than in clean days, especially for the first two haze events (the O_3 concentrations in the third haze event was relatively lower due to the higher NO_x concentrations in the urban area).

The observed $PM_{2.5}$ and nitrate trends at the BUCT site were well simulated

288　**(Fig.2a&b)**, and NO_2 simulations generally agreed with the observations **(Fig.2c)**.

289　The promotion effect of the six potential HONO sources on the formation of

290　secondary aerosols leads to an increase in concentrations of $PM_{2.5}$ and nitrate for case

291　6S, despite nitrate consumption through $Phot_{nitrate}$ (Li et al., 2010; Qu et al., 2019; Fu

292　et al., 2019; Zhang et al., 2019a, 2021), detailed nitrate variation caused by each of

293　the six potential HONO sources in case 6S is presented in **Fig.S3**. The overestimation

294　of nitrate could be partially caused by the uncertainties in the anthropogenic emission

295　inventory, e.g., the overestimation of NO_x emissions **(Fig.2c)**. The inadequate

296　understanding of the nitrate formation mechanism could also be related to nitrate

297　simulation bias, which was also found in some related studies using CMAQ (Fu et al.,

298　2019; Zhang et al., 2021).

299　　　Hourly and diurnal HONO simulations at the BUCT site **(Fig.2d&3a)** were

300　significantly improved in the 6S case (mean is 1.47 ppb) compared with the base case

301　(mean is 0.05 ppb). The normalized mean bias (NMB) was remarkably reduced to

302　-14.22% (6S) from -97.11% (Base), and the index of agreement (IOA) was improved

303　significantly to 0.80 (6S) from 0.45 (Base) **(Fig.2d)**. The underestimation of the

304　simulated HONO (6S) on Oct.15 and Oct.22 was mainly caused by the earlier

305　scavenging of pollutants at the BUCT site in the used model **(Fig.2a&d)**.

306　　　As for O_3, noticeable improvements could be found at the BUCT site after

307　considering the six potential HONO sources, especially in hazy days **(Fig.2e&f)**. The

308　mean bias (MB) was improved to -3.61 ppb (6S) from -7.09 ppb (Base), and the IOA

309　was improved to 0.86 (6S) from 0.78 (Base) **(Fig.2e)**. Specially, the 6S case

significantly enhanced daytime hourly O_3 by 15–35 ppb compared with the base case

and the simulated O_3 was very close to the observations in hazy days (**Fig.2e**). Larger

daytime O_3 enhancements were accompanied with higher $PM_{2.5}$ concentrations during

haze aggravating processes, while in clean days the daytime enhanced O_3 due to the

potential HONO sources was mostly < 5 ppb (**Fig.2e&f**). The diurnal O_3 pattern

during the first two haze aggravating processes is presented in **Fig.3b**, significant

improvements in daily maximum 8-h (10:00–17:59) averaged (DMA8) O_3 (18.8 ppb)

occurred at the BUCT site after considering the six potential HONO sources, and the

NMB of DMA8 O_3 was remarkably improved to -2.38% (6S) from -47.14% (Base).
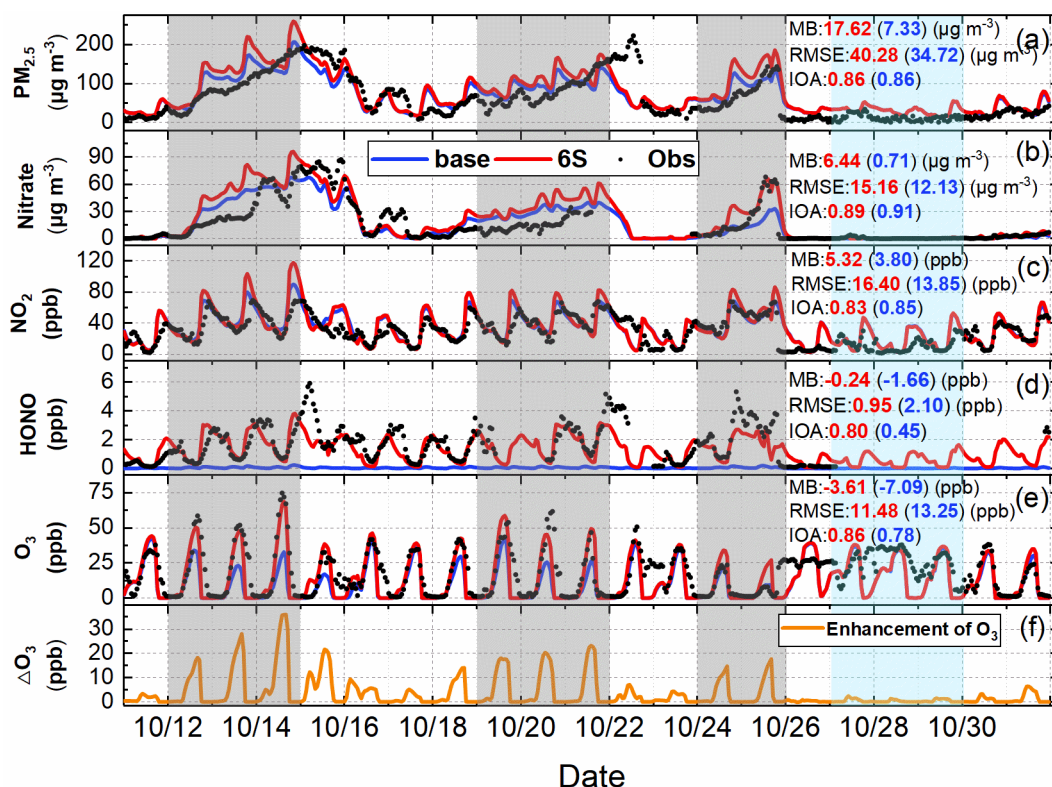
Figure 2 Comparison of simulated (Base and 6S cases) and observed hourly concentrations of

$PM_{2.5}$, nitrate, NO_2, HONO and O_3 (a–e), and the hourly enhanced concentrations of O_3 ($\triangle O_3$) (f)

caused by the six potential HONO sources (6S minus Base) at the BUCT site during Oct.11–31 of

16

324   2018.

325

326
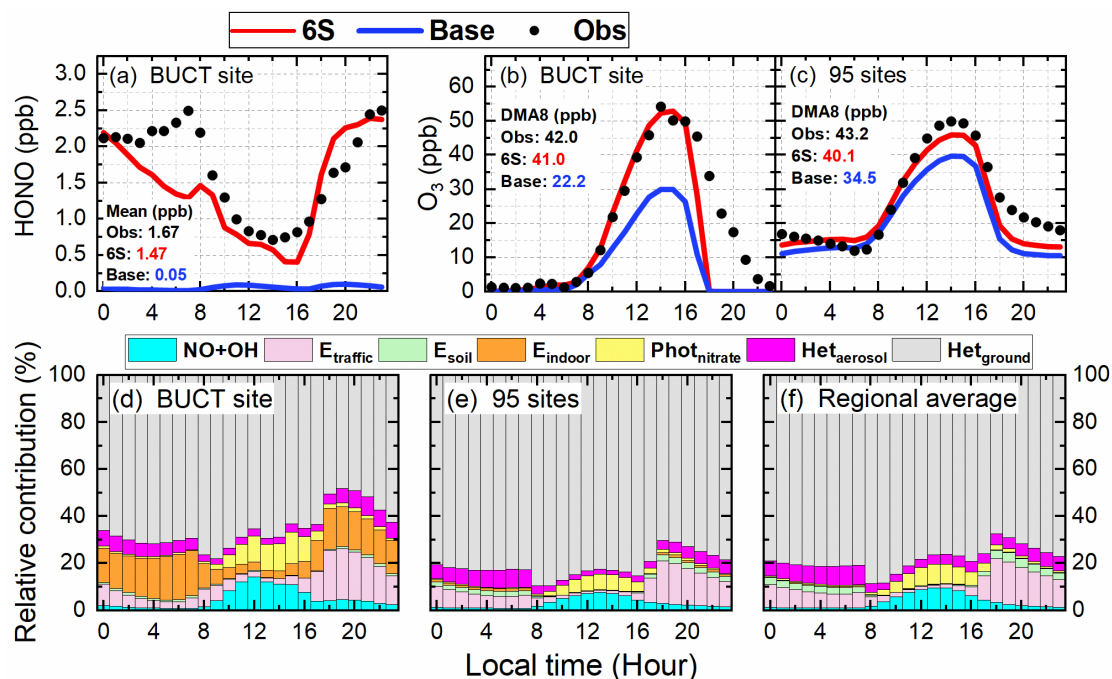
Figure 3 Comparison of diurnal mean simulations (Base and 6S cases) and observations of HONO during the study period (a) and O_3 during the first two haze events at the BUCT site (b), and O_3 averages at the 95 NCP monitoring sites during the study period (c); and the relative contributions of each of the six potential HONO sources and the reaction of OH with NO to surface HONO concentrations for the 6S case at the BUCT site (d), at the 95 monitoring sites (e) and in the whole NCP region (f) (The calculated 24-h mean HONO concentrations and DMA8 O_3 concentrations were given in panels (a) – (c)).

335

336   The relative contribution of each HONO source near the surface at the BUCT site

337   for the 6S case is shown in **Fig.3d**. Briefly, Het_{ground} was the largest source during

338   daytime and nighttime (~50–70%), consistent with the results of Zhang et al. (2021).

17

339 Phot$_{nitrate}$ ($J_{nitrate}/J_{HNO3}$ = 30) and the NO+OH reaction contributed similarly ~1–12%

340 during daytime. E$_{traffic}$ was important during nighttime (~10–20%) but small during

341 daytime (<5%). The contribution of Het$_{aerosol}$ to HONO concentrations was minor

342 (~2–3%) in daytime and ~6–10% in nighttime. E$_{soil}$ could be neglected while the

343 contribution of E$_{indoor}$ was close to that of E$_{traffic}$ in urban Beijing. The relative

344 contribution of the potential HONO sources in this study was comparable with the

345 result of Fu et al. (2019) by using CMAQ, except for the contribution of Phot$_{nitrate}$ due

346 to the different $J_{nitrate}/J_{HNO3}$ ratios (30 in our study and ~120 in Fu et al. (2019)).

347

348 **3.1.3 Pollutant concentrations in NCP**

349 The 95-site-averaged hourly simulations and observations of O$_3$, NO$_2$ and PM$_{2.5}$

350 during the study period are shown in **Fig.4**. The six potential HONO sources

351 significantly improved hourly O$_3$ simulations, remarkably enhanced the daily

352 maximum O$_3$ by ~5–10 ppb during Oct. 11–25, and by ~2–4 ppb during Oct. 26–31

353 (**Fig.4a&b**). The simulations of NO$_2$ well agreed with the observations, and the mean

354 concentrations were 22.55 (Base), 21.62 (6S) and 20.74 (Obs) ppb (**Fig.4c**). The

355 PM$_{2.5}$ simulations generally followed the observed PM$_{2.5}$ trend but were

356 overestimated by ~8 μg m^{-3}, with averaged concentrations of 49.94 (Base), 53.30 (6S)

357 and 45.31 (Obs) μg m^{-3} (**Fig.4d**), respectively.

358
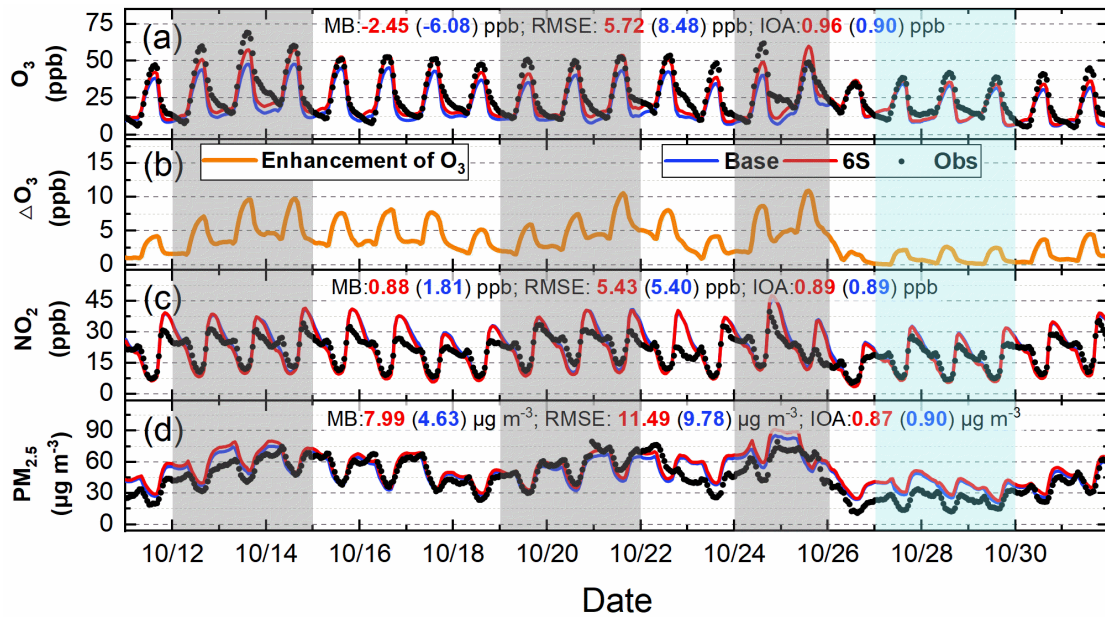
Figure 4 Comparison of 95-site-averaged hourly simulations (Base and 6S cases) and observations of

O_3(a), NO_2 (c) and $PM_{2.5}$ (d), and O_3 enhancements due to the six potential HONO sources (6S minus

Base case) (b) in the North China Plain during Oct.11–31 of 2018.

The 95-site-averaged diurnal simulations and observations of O_3 are presented in

Fig.3c, O_3 simulations showed a remarkable improvement when the six potential

HONO sources were considered, the six potential HONO sources produced a mean

enhancement of 5.7 ppb in DMA8 O_3 and improved the NMB to -7.16% from -20.32%

at the 95 sites in NCP. The 95-site-averaged diurnal simulations and observations of

NO_2 and $PM_{2.5}$ during the study period are demonstrated in **Fig.S4**. NO_2 simulations

generally followed the observed trend but were underestimated during 04:00 to 16:00

and overestimated after 18:00 (**Fig.S4a**), $PM_{2.5}$ simulations agreed with the observed

diurnal pattern but were overestimated for both cases during the whole day (**Fig.S4b**).

The relative contribution of each HONO source near the surface at the 95 NCP

sites for the 6S case is shown in **Fig.3e.** Het_{ground} was the dominant source during

375 daytime and nighttime (~70–80%). Phot$_{nitrate}$ (J$_{nitrate}$/J$_{HNO3}$ = 30) and the NO+OH

376 reaction nearly equaled and contributed ~2–8% during daytime (~5% on average).

377 E$_{traffic}$ was important during nighttime (~10–15%) but small during daytime (<3%).

378 The contribution of Het$_{aerosol}$ to HONO concentrations was <3% in daytime and <10%

379 in nighttime. E$_{soil}$ contributed ~3% in nighttime but could be neglected in daytime.

380 The contribution of E$_{indoor}$ was too small to be noticed at the 95 NCP sites, implying

381 that this source was noticeable only in megacities. The relative contribution of each

382 HONO source in the whole NCP region (all grid cells in domain two except for the

383 seas) is presented in **Fig.3f**, the results were quite similar with those at the 95 sites

384 (**Fig.3f**), which were representative for the whole NCP region. To further understand

385 the role of potential HONO sources in haze aggravating processes in regional O$_3$

386 concentrations, the 95 site-averaged surface/vertical HONO concentrations and their

387 impacts during a typical haze event (Oct. 19–21) and a clean period (Oct. 27–29) were

388 analyzed and are shown in the following sections.

389

390 **3.2 Spatial distribution of enhanced DMA8 O$_3$ by potential HONO sources**

391 **3.2.1 General patterns of enhanced DMA8 O$_3$**

392 **Fig.S5** shows surface-averaged and zonal-averaged DMA8 O$_3$ enhancements due

393 to the six potential HONO sources in NCP during the study period (Oct.11-31) and

394 three haze events (Oct.12–14, Oct.18–21 and Oct.24–25). The overall surface DMA8

395 O$_3$ enhancement decreased gradually from south (6–10 ppb) to north (2–6 ppb)

396   (**Fig.S5a**) and could reach 10–20 ppb under unfavorable meteorological conditions

397   during haze events (**Fig.S5b–d**). For the first two haze events, the anti-cyclone in the

398   Shandong peninsula carried pollutants being transported from the southeastern NCP

399   to the western (108–112°E) and northern (39–41°N) NCP, and the six potential

400   HONO sources led to a DMA8 O_3 enhancement of 10–20 ppb (**Fig.S5b**) and 10–15

401   ppb (**Fig.S5c**) in Beijing, respectively. For the third haze event, two air masses were

402   converged to form a transport channel from south to north, the O_3 enhancement

403   caused by the six potential HONO sources can reach 10–18 ppb in the southern NCP

404   and decreased to 6–10 ppb in the northern NCP along the transport channel. Vertically,

405   the DMA8 O_3 enhancements were 2–8 ppb during the whole period (**Fig.S5e**) and

406   increased to 6–12 ppb in these haze events (**Fig.S5f–h**). The enhanced O_3 near the

407   surface (0–100 m) was slightly smaller than that at higher altitude (**Fig.S5f–h**), due

408   mainly to the stronger titration of O_3 by NO near the surface. The above results

409   demonstrated that the six potential HONO sources significantly enhanced surface and

410   vertical O_3 concentrations in NCP, especially during haze events.

411

412   **3.2.2 During a typical haze aggravating process and a clean period**

413   **Fig.5** demonstrates surface-averaged and zonally-averaged DMA8 O_3

414   enhancements due to the six potential HONO sources in NCP during a typical haze

415   aggravating process (Oct.19–21, 2018) and a clean period (Oct.27–29, 2018). The

416   increasing trend of DMA8 O_3 enhancements can be clearly seen from Oct.19 to

417   Oct.21 near the surface and in the vertical direction. During the haze aggravating

418   process, the surface DMA8 O_3 enhancements were ~2–10 ppb (Oct.19), ~6–12 ppb

419   (Oct.20) and ~8–15 ppb (Oct.21), respectively; the vertical DMA8 O_3 enhancements

420   were ~4–7 ppb (Oct.19), ~6–10 ppb (Oct.20), and ~8–15 ppb (Oct.21), respectively.

421   While during clean days, the surface/vertical DMA8 O_3 enhancements were usually

422   <4 ppb. The six potential HONO sources significantly enhanced surface and vertical

423   O_3 concentrations in NCP during haze aggravating processes, the detailed role of the

424   potential HONO sources on vertical HONO concentrations and their impacts are

425   presented in the next section.

426

427

428

22
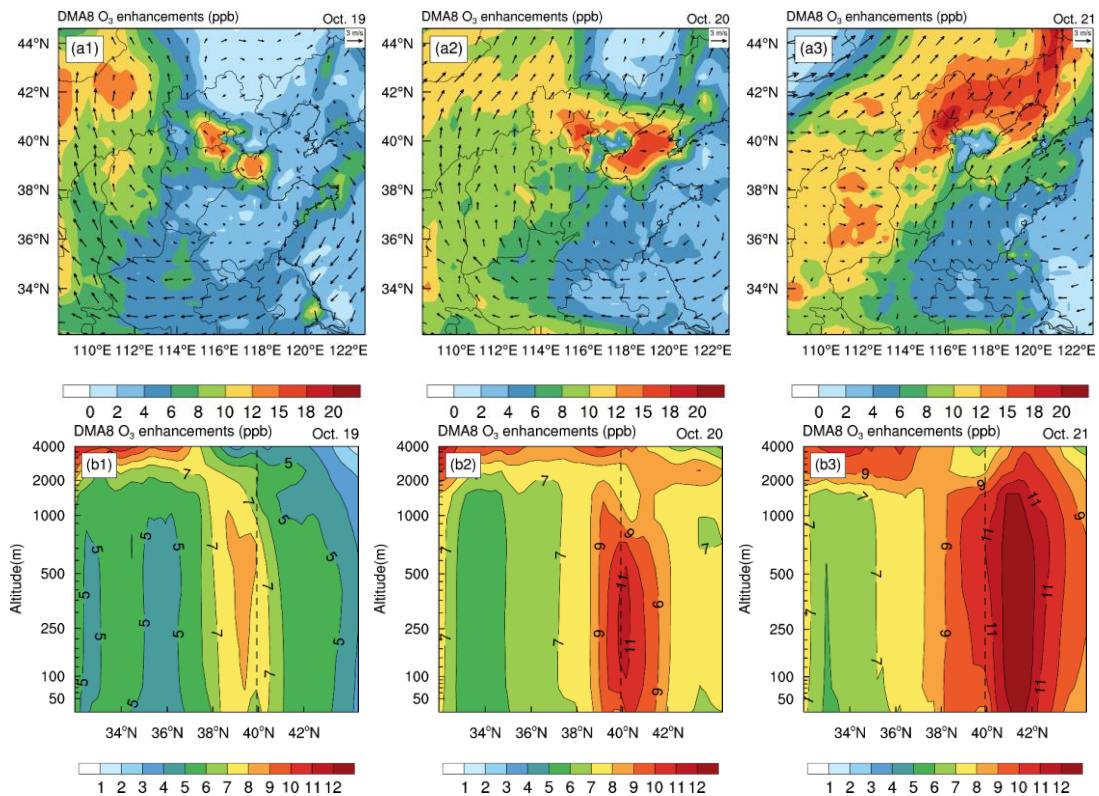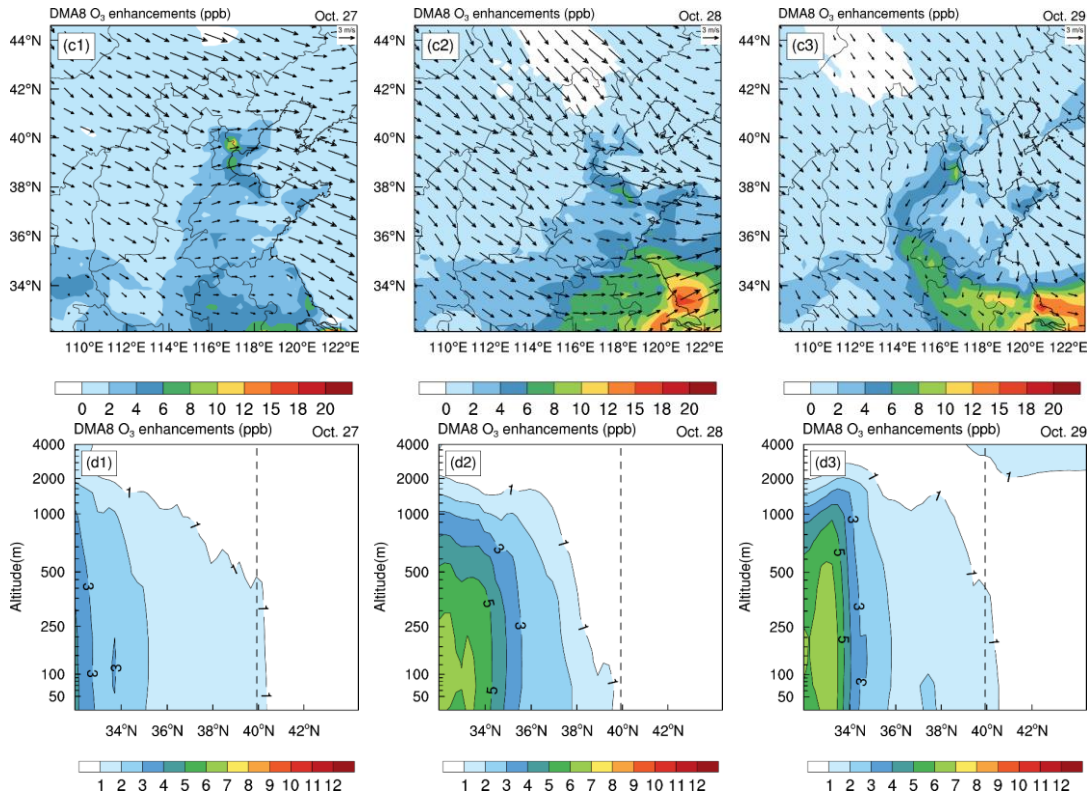
Figure 5 Surface-averaged (a1–a3, c1–c3) and zonal-averaged (b1–b3, d1–d3) DMA8 O_3 enhancements due to the six potential HONO sources in the North China Plain during a typical haze aggravating process (Oct.19–21, 2018) and a clean period (Oct.27–29, 2018) (The dashed line denotes the latitude of the BUCT site).

3.3 Vertical variations of the six potential HONO sources and their impacts

3.3.1 Six potential HONO sources and their impacts on HONO concentrations

A number of studies have conducted vertical HONO observations abroad (Kleffmann et al., 2003; Ryan et al., 2018; Sorgel et al., 2011; VandenBoer et al., 2013; Villena et al., 2011; Wang et al., 2020; Wong et al., 2011, 2012; Zhang et al., 2009) and in China (Meng et al., 2020; Wang et al., 2019; Xing et al., 2021; Zhu et al., 2011).

442　A decreasing trend of HONO with height was mostly observed among these studies,

443　and our simulations also reproduced this vertical variation and were comparable with

444　another model simulation by Zhang et al. (2021) who used CMAQ (**Fig.S6**). For a

445　deep understanding of the role of each considered HONO source in HONO

446　concentrations at different heights, we assessed the contributions of each potential

447　HONO source to HONO concentrations at different heights (**Fig.6**) during Oct.11–31

448　of 2018.

449　　　　Generally, the impacts of ground-based potential HONO sources ($E_{traffic}$, E_{soil},

450　E_{indoor} and Het_{ground}) on HONO concentrations decreased rapidly with height, while

451　the NO+OH reaction and aerosol related HONO sources ($Phot_{nitrate}$ and $Het_{aerosol}$)

452　decreased slowly with height (**Fig.6**). During daytime the NO+OH reaction, $Phot_{nitrate}$

453　and Het_{ground} were the three main HONO sources, while during nighttime $E_{traffic}$,

454　$Het_{aerosol}$ and Het_{ground} were the three main contributors to HONO concentrations

455　(**Fig.6**). The HONO concentrations via the NO+OH reaction and $Phot_{nitrate}$ were

456　higher during daytime. The impact of E_{soil} in the NCP was small, nevertheless, Xue et

457　al. (2021) found strong soil HONO emissions in NCP agricultural fields after

458　fertilization, suggesting that this source may have a remarkable enhancement on

459　regional HONO and secondary pollutants in crop growing seasons.

460
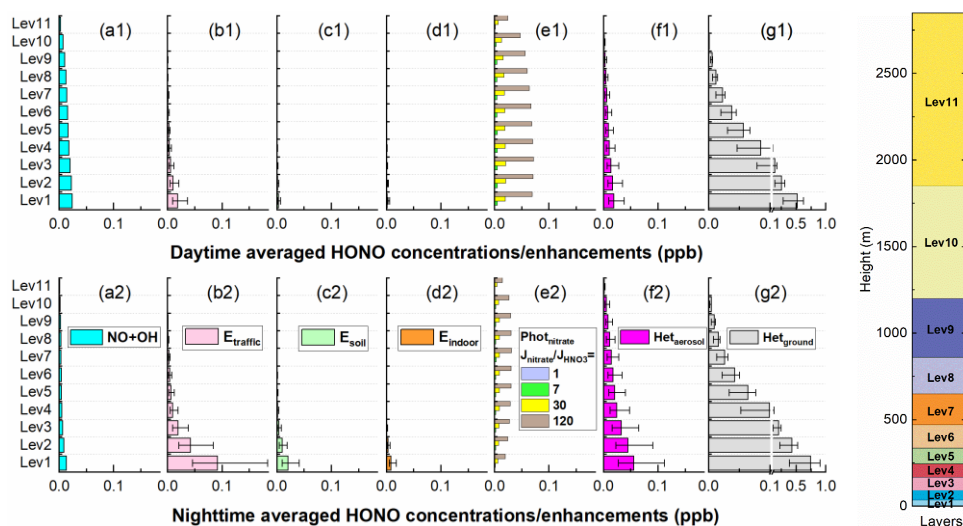
Figure 6 The 95-site-averaged daytime/nighttime HONO concentrations/enhancements at different heights when the NO+OH reaction (a1&a2) and each of the six potential HONO sources (b1–g1&b2–g2) were considered during Oct.11–31 of 2018 (The error bar denotes the uncertainties of each potential HONO source in HONO concentrations (**Table 2**). The right panel denotes the approximate height of each vertical layer above the ground).

The comparison of HONO concentrations/enhancements during a haze aggravating process and a clean period is shown in **Figs.7&8**. Generally, daytime HONO concentrations increased in haze aggravating processes and were higher than those in clean days. Het_{ground} was the dominant source of the surface HONO in both hazy and clean days and contributed 80–90% of daytime averaged HONO concentrations (**Fig.8**), however, this reaction occurred only on the ground surface, thus its relative contribution decreased with height, especially in haze aggravating processes (**Fig.8**). Although the contribution of the NO+OH reaction to daytime HONO was small near the surface, its relative contribution to HONO increased with height, especially in clean days (**Fig.8**). As for $Phot_{nitrate}$, a much larger enhancement

25

478　could be found in hazy days compared with clean days. In clean days the daytime

479　enhanced HONO by $Phot_{nitrate}$ was only 1–3 ppt in general and its contribution to

480　daytime HONO was usually <10%, while in the haze aggravating process, the

481　enhanced HONO concentration by $Phot_{nitrate}$ was about ten times higher than that in

482　clean days and $Phot_{nitrate}$ became the dominant HONO source (~30–70%) at higher

483　altitude, and both HONO concentrations and contributions by $Phot_{nitrate}$ increased with

484　the air pollution aggravation (**Fig.7a–c, Fig.8a–c**). The contributions of direct

485　emission sources were small and decreased when $PM_{2.5}$ increased, compared with

486　those heterogeneous reactions. Higher concentrations of NO_2, nitrate, and $PM_{2.5}$

487　favored heterogeneous formation of HONO, while direct emission sources were

488　relatively invariable under different pollution levels.

489　　Based on our results, nitrate concentrations increased with the haze aggravating

490　processes (**Fig.2b**), as a positive feedback effect, the elevated nitrate could in turn

491　enhance HONO formation and further enhance the atmospheric oxidation capacity

492　during daytime. Considering $J_{nitrate}$ was still unclear, sensitivity tests were conducted

493　and are presented in the discussion section.

494
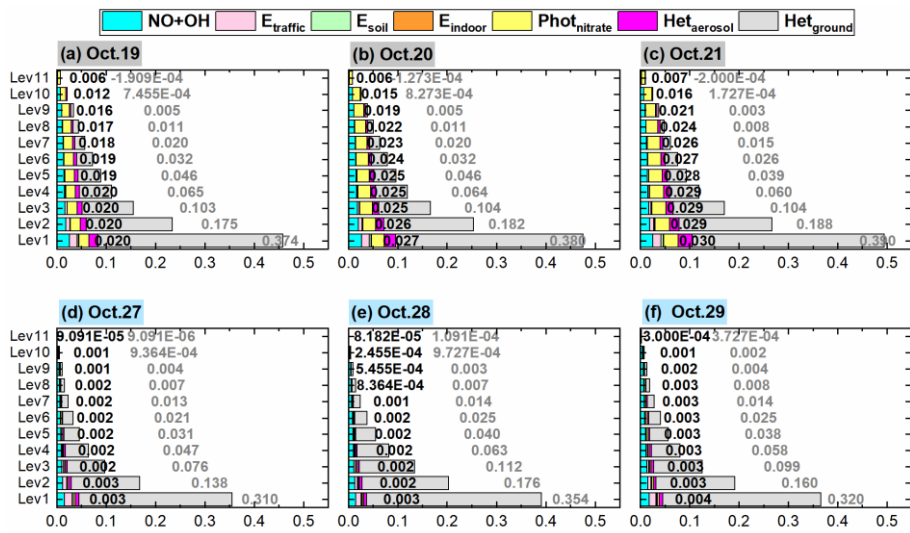
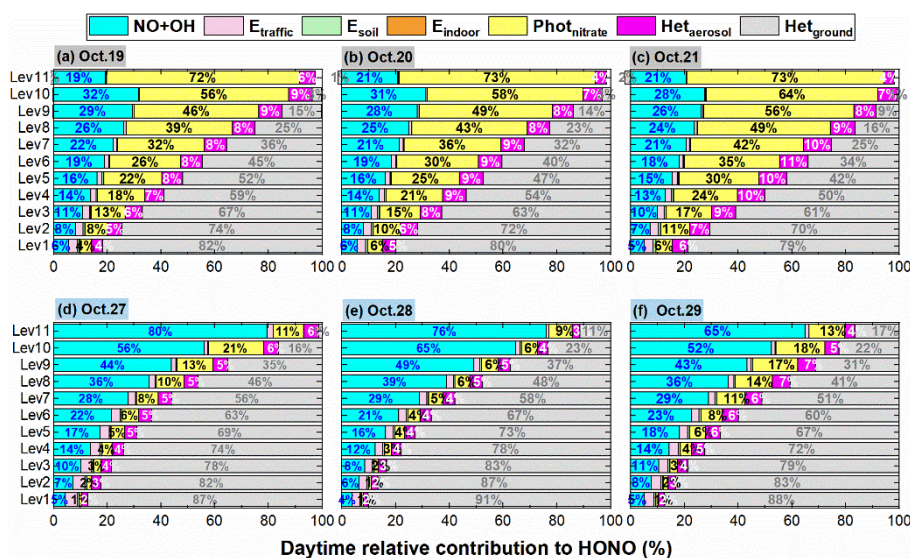**Figure 7** The 95-NCP-site-averaged daytime HONO concentrations at different heights when the NO+OH reaction and the six potential HONO sources were included during a typical haze aggravating process of Oct.19–21 (a–c) and a clean period of Oct.27–29 (d–f) of 2018 (The first column numbers in black in each graph are for Phot$_{nitrate}$, and the second column numbers in gray are for Het$_{ground}$).

Figure 8 The 95-NCP-site-averaged relative contributions of the NO+OH reaction and each of the six potential HONO sources to daytime HONO concentrations at different heights during a typical

27

505   haze aggravating process of Oct.19–21 (a–c) and a clean period of Oct.27–29 (d–f) of 2018 (The

506   first column numbers in blue in each graph are for the NO+OH reaction, the second column

507   numbers in black are for $Phot_{nitrate}$, the third column numbers in white are for $Het_{aerosol}$, and the

508   fourth column numbers in gray are for Het_{ground}).

509

510   **3.3.2 Enhanced OH and its production rate**

511   **Fig.9** demonstrates daytime variations of OH production (P(OH)) and loss

512   (L(OH)) rates near the surface and in the vertically-averaged layer (from ground to

513   the height of 2.5km) at the 95 NCP sites for the Base and 6S cases during Oct.11–31,

514   2018. A significant enhancement of P/L(OH) can be found near the surface and

515   vertically, the six potential HONO sources accelerated OH production and loss rates

516   remarkably near the surface and noticeably in the considered vertical layers.

517   Near the surface, daytime P(OH) and L(OH) were significantly enhanced by~320%

518   for the 6S case (mean was 5.27 ppb h^{-1}) compared with the base case (mean was 1.26

519   ppb h^{-1}). For the base case, the daytime P(OH) via the photolysis of HONO and O_3

520   was 0.09 ppb h^{-1} and 0.09 ppb h^{-1}, respectively, while the daytime L(OH) via the

521   NO+OH reaction was 0.11 ppb h^{-1} and the net contribution of HONO photolysis to

522   P(OH) was -0.02 ppb h^{-1}. After adding the six potential HONO sources in case 6S, the

523   daytime P(OH) via the photolysis of HONO and O_3 was 1.81 ppb h^{-1} and 0.10 ppb h^{-1},

524   respectively, the daytime L(OH) via the NO+OH reaction was 0.48 ppb h^{-1} and the net

525   contribution of HONO photolysis to P(OH) reached 1.33 ppb h^{-1}. HONO photolysis

was the main source of the primary formation of OH, while the secondary formed OH

via the reaction of HO_2+NO (3.14 ppb h^{-1}) was the dominant source of the total OH

formation.

Vertically, daytime P(OH) or L(OH) was enhanced by ~105% for the 6S case

(mean was 2.21 ppb h^{-1}) compared with the base case (mean was 1.08 ppb h^{-1}). For

the base case, the daytime P(OH) via the photolysis of HONO and O_3 was 0.06 ppb

h^{-1} and 0.10 ppb h^{-1}, respectively, while the daytime L(OH) via the NO+OH reaction

was 0.07 ppb h^{-1} and the net contribution of HONO photolysis to P(OH) was -0.01

ppb h^{-1}. After coupling the six potential HONO sources in case 6S, the daytime P(OH)

via the photolysis of HONO and O_3 and via the HO_2+NO reaction was 0.48 ppb h^{-1},

0.12 ppb h^{-1} and 1.52 ppb h^{-1}, respectively, the daytime L(OH) via the NO+OH

reaction was 0.15 ppb h^{-1} and the net contribution of HONO photolysis to P(OH) was
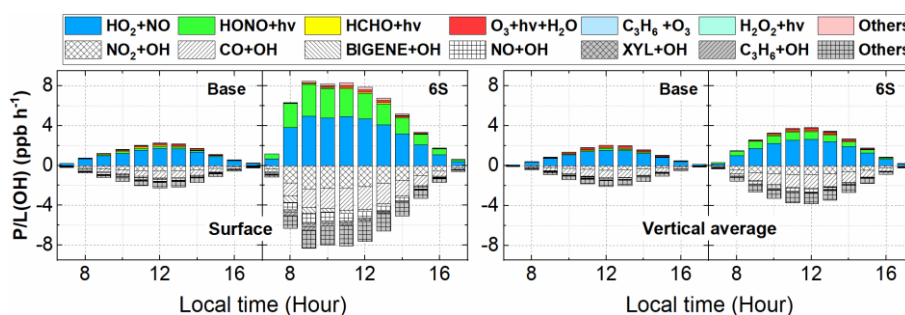
0.33 ppb h^{-1}.

Figure 9 Diurnal mean variations of OH production (P(OH)) and loss (L(OH)) rates including

major production and loss reactions near the surface and in the vertically-averaged layer (from

ground to the height of 2.5km) at the 95 NCP sites for the Base and 6S cases during Oct.11–31,

2018.

545

546   **Fig.10** shows the linear relationships between daytime-averaged P(OH) and

547    $PM_{2.5}$ concentrations and between daytime-averaged OH and $PM_{2.5}$ concentrations

548   from ground to the height of 2.5km at the 95 NCP sites during Oct. 11–31 of 2018.

549   Both P(OH) for the two cases (Base and 6S) and the enhanced P(OH) due to the six

550   potential HONO sources showed a strong positive correlation (r>0.8) with $PM_{2.5}$

551   concentrations at the 95 NCP sites, because $Het_{aerosol}$, Het_{ground} and $Phot_{nitrate}$ were

552   significantly increased with the elevated $PM_{2.5}$. The enhanced P(OH) for the 6S case

553   reached 0.043 ppb h^{-1} per 1μg m^{-3} of a $PM_{2.5}$ enhancement. Similarly, high positive

554   correlation (r>0.6) could be found between OH and $PM_{2.5}$ concentrations, the OH

555   concentrations and enhancements due to the six potential HONO sources were both

556   higher in hazy days than those in clean days, and the enhancement of OH reached

557   3.62×10^4 molec cm^{-3} per μg m^{-3} of $PM_{2.5}$ for case 6S. These results were consistent

558   with a recent field study reported by Slater et al. (2020), who found that the OH

559   observed in haze events was elevated in central Beijing in November–December of

560   2016. Furthermore, two observations confirmed the key role of HONO in producing

561   primary OH despite the relatively lower photolysis frequency in haze aggravating

562   processes (Slater et al., 2020; Tan et al., 2018), consistent with our simulations

563   (**Fig.S7** shows the relationship between surface $PM_{2.5}$ and photolysis frequencies of

564   NO_2, HONO and HNO_3 in this study,).
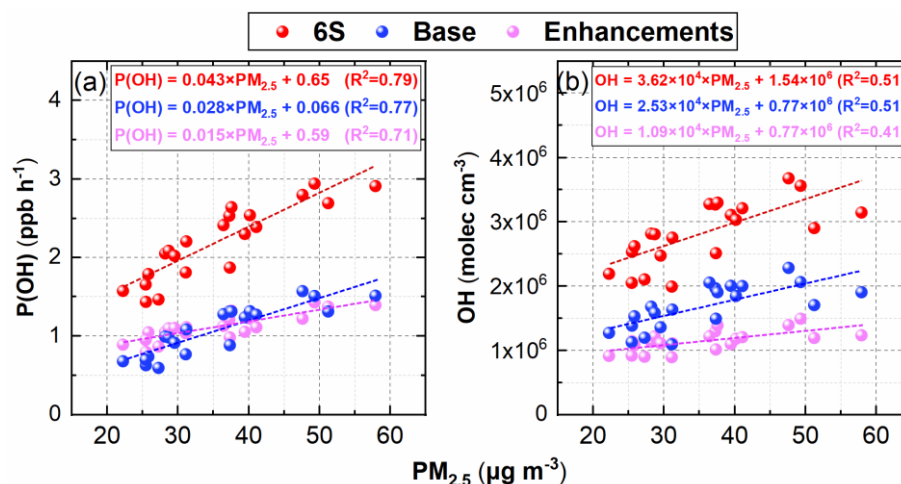
Figure 10 The linear relationships between daytime-averaged P(OH) and $PM_{2.5}$ concentrations (a) and between daytime-averaged OH and $PM_{2.5}$ concentrations (b) from ground to the height of 2.5km at the 95 NCP sites during Oct. 11–31 of 2018.

Figs.11&12 show the detailed comparisons of P(OH) and OH enhancements during a haze aggravating process and a clean period. It can be seen that both P(OH) and OH were enhanced in hazy days compared with clean days, and P(OH) and OH increased with the aggravated haze pollution. Among the six potential HONO sources, Het_{ground} was the largest contributor to the enhanced P(OH) and OH near the surface, but its contribution was relatively stable under different pollution levels and was attenuated rapidly with height in both hazy and clean days; the contribution induced by $Phot_{nitrate}$ was remarkably increased in haze aggravating processes and was about ten times higher than that in clean days; $Het_{aerosol}$ also increased with the pollution levels but with relatively small values, while the impact of other three direct emission sources of HONO was quite small.
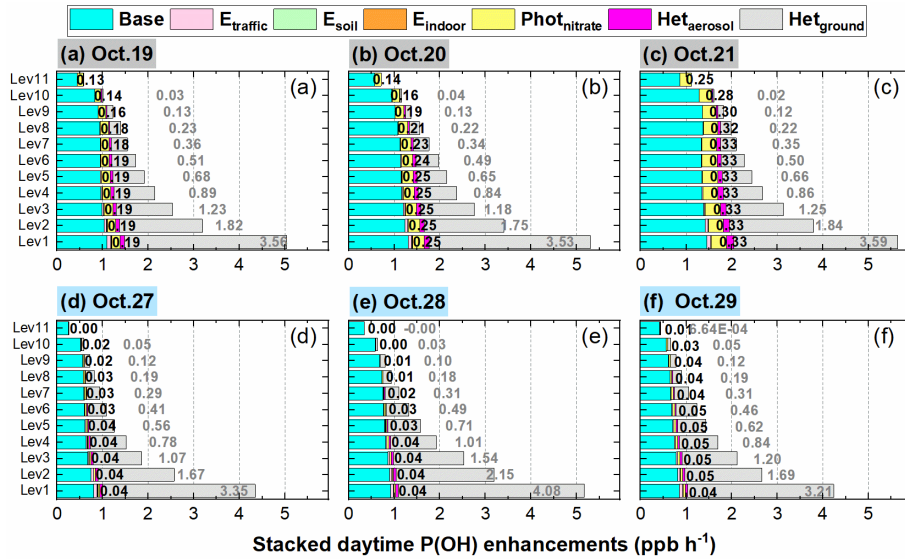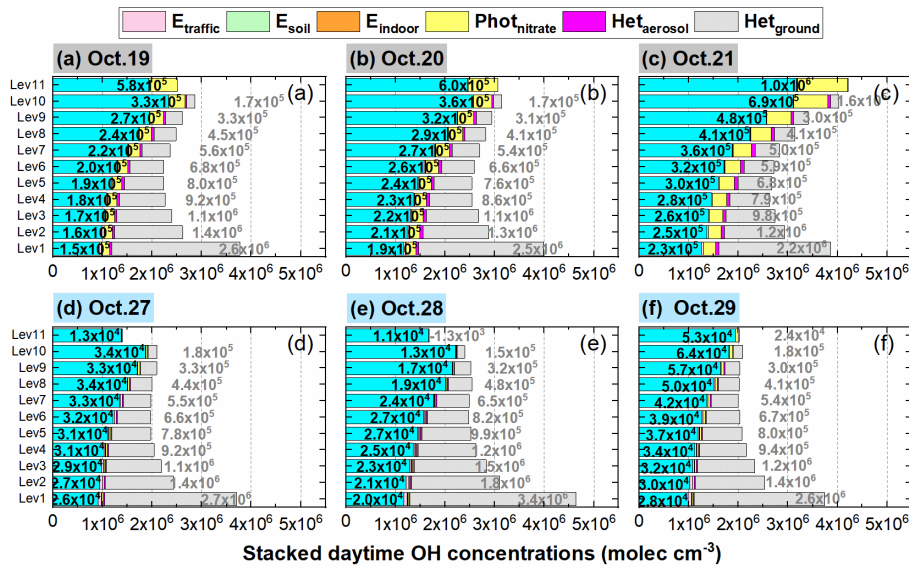
582

583 **Figure 11** The 95-NCP-site-averaged daytime P(OH) for the base case and the enhancements due

584 to the six potential HONO sources during a typical haze aggravating process of Oct.19–21 (a–c)

585 and a clean period of Oct.27–29 (d–f) of 2018 (The first column number in black in each graph is

586 for Phot$_{nitrate}$, and the second column number in gray is for Het$_{ground}$).

587

588

589 **Figure 12** The 95-NCP-site-averaged daytime OH concentrations for the base case and the

590 enhancements due to the six potential HONO sources during a typical haze aggravating process of

591 Oct.19–21 (a–c) and a clean period of Oct.27–29 (d–f) of 2018 (The first column number in black

592   in each graph is for $Phot_{nitrate}$, and the second column number in gray is for Het_{ground}).

593

3.3.3 Enhanced DMA8 O_3

595   **Fig.13** demonstrates the linear relationship between DMA8 O_3 enhancements and

596   daytime $PM_{2.5}$ concentrations in each vertical layer and the averaged vertical layer for

597   the considered eleven layers at the 95 NCP sites during Oct. 11–31 of 2018. A good

598   correlation ($r>0.8$) between DMA8 O_3 enhancements and daytime $PM_{2.5}$

599   concentrations in the vertical averaged layer (similar reasons for the strong positive

600   correlation between the enhanced P(OH) and $PM_{2.5}$ concentrations shown above)

601   suggests that the enhanced O_3 due to the six potential HONO sources was larger in

602   polluted days and increased during the haze aggravating processes. The enhanced

603   DMA8 O_3 was < 2ppb when $PM_{2.5}$ was < 20μg m^{-3} and was >10 ppb when $PM_{2.5}$ was >

604   60μg m^{-3} on average, with a mean DMA8 O_3 enhancement of 0.24 ppb per μg m^{-3} of

605    $PM_{2.5}$.

606
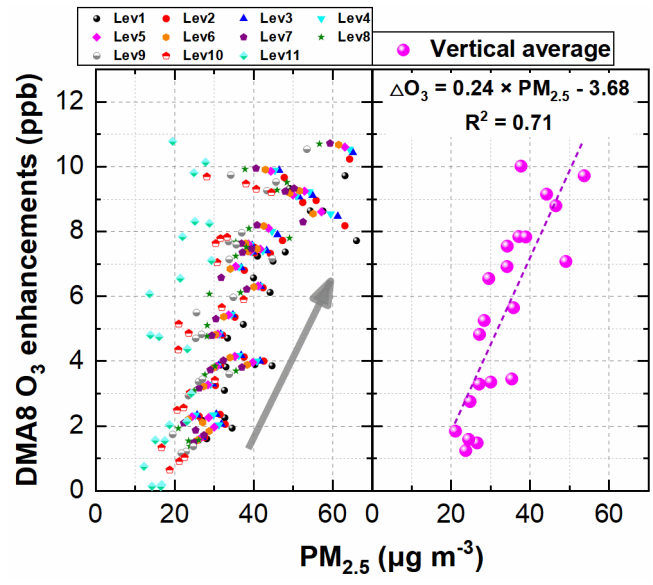
Figure 13 The linear relationship between DMA8 O₃ enhancements and daytime PM₂.₅ concentrations in each vertical layer (a) and the averaged vertical layer for the considered eleven layers (b) at the 95 NCP sites during Oct. 11–31 of 2018.
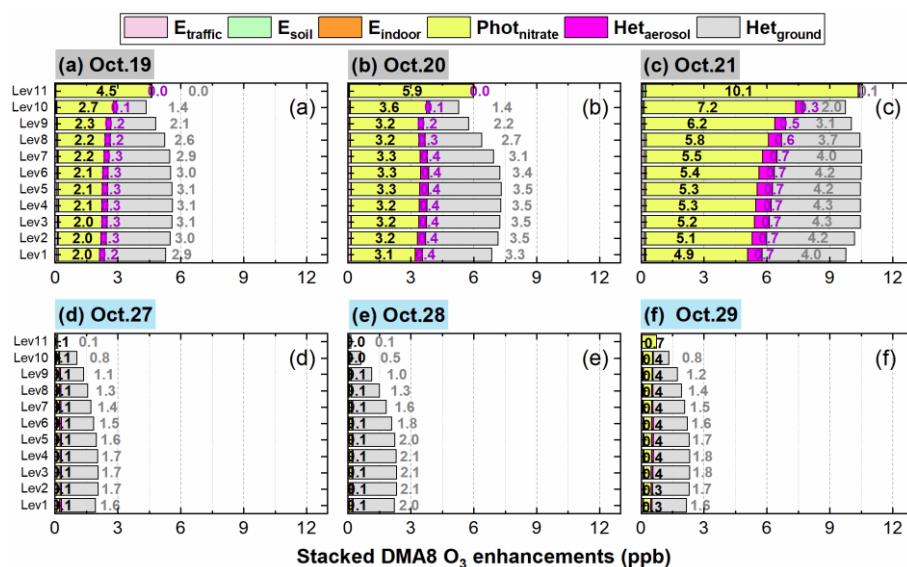
Fig.14 shows the 95-NCP-site-averaged DMA8 O₃ enhancements due to the six potential HONO sources during a typical haze aggravating process of Oct.19–21 and a clean period of Oct.27–29 of 2018. A significant enhancement of DMA8 O₃ can be found during the haze aggravating process compared with during clean days. The enhanced DMA8 O₃ was ~5.5 ppb (Oct.19), ~ 7 ppb (Oct.20) and ~ 10 ppb (Oct.21), respectively, during the haze aggravating process, while that was usually ~2 ppb in clean days.

In clean days, Het$_{ground}$ was the dominant contributor (~1.5–2 ppb) to the enhanced DMA8 O₃ among the six potential HONO sources, the contribution of Phot$_{nitrate}$ to the enhanced DMA8 O₃ was ~0.1–0.4 ppb, while that of the other four sources was minor. When it comes to the comparison between the haze aggravating

process (Oct.19–21) and clean days, the DMA8 O_3 enhancements induced by Het_{ground}

were doubled and reached ~3–4 ppb; the contribution of $Phot_{nitrate}$ to the enhanced

DMA8 O_3 substantially increased and reached ~2–4.5 ppb (Oct.19), ~3–6 ppb (Oct.20)

and ~5–10 ppb (Oct.21), respectively; $Het_{aerosol}$ showed an increasing contribution to

the enhanced DMA8 O_3 during haze aggravating process (~0.3 ppb on Oct.19, ~0.4

ppb on Oct.20 and ~0.7 ppb on Oct.21), while the impacts of the other three direct

emission sources ($E_{traffic}$, E_{soil}, and E_{indoor}) on the enhanced DMA8 O_3 were minor.

Figure 14 The 95-NCP-site-averaged DMA8 O_3 enhancements due to the six potential HONO

sources during a typical haze aggravating process of Oct.19–21 (a–c) and a clean period of

Oct.27–29 (d–f) of 2018 (The column in black numbers in each graph is for $Phot_{nitrate}$, the column

in purple numbers in each graph is for $Het_{aerosol}$, and the column in gray numbers is for Het_{ground}).

3.4 Vertical variations of O_3-NO_x-VOCs sensitivity

Based on the results above, $Phot_{nitrate}$ could significantly enhance the DMA8 O_3 by ten times in the considered vertical layers (especially at elevated heights) in polluted events, but previous studies have not fully discussed. To better understand its role in vertical O_3 formation, the O_3-NO_x-VOCs sensitivity was analyzed by using the $P(H_2O_2)/P(HNO_3)$ ratio proposed by Sillman (1995), which is more suitable than the concentration ratio of H_2O_2/HNO_3 because of the large dry deposition velocity of the two gases in the troposphere (Sillman, 1995). A transition point of $P(H_2O_2)/P(HNO_3)$ = 0.35 was suggested by Sillman (1995), when $P(H_2O_2)/P(HNO_3)$ was <0.35, O_3 shows VOCs-sensitive chemistry (increasing VOC concentrations can significantly elevate O_3 levels) and when $P(H_2O_2)/P(HNO_3)$ was >0.35, O_3 tends to NO_x-sensitive chemistry (increasing NO_x concentrations can significantly elevate O_3 levels).

Fig.15 demonstrates the 95-NCP-site-averaged $P(H_2O_2)/P(HNO_3)$ ratio at each vertical layer for the 6S case during a typical haze aggravating process of Oct.19–21 and a clean period of Oct.27–29 of 2018. Obviously opposite O_3 sensitivity appeared between the lower layers (VOCs sensitive) and the higher layers (NO_x sensitive) in both clean and hazy days, and the transition point usually appeared at the eighth layer (~600–800 m).

The $Phot_{nitrate}$ reaction is assumed to produce HONO and NO_x (Zhou et al., 2003; Romer et al., 2018; Gen et al., 2022), this reaction not only enhances OH concentrations via HONO photolysis, but also directly releases NO_x back into the troposphere. Considering the NO_x-sensitive O_3 chemistry at higher layers (>800m),

659 elevating OH and NO_x concentrations are both favorable for O_3 formation, especially

660 in haze aggravating processes with abundant nitrate (detailed vertically enhanced O_3

661 production/loss rates induced by $Phot_{nitrate}$ are shown in **Fig.S8**).

662

663
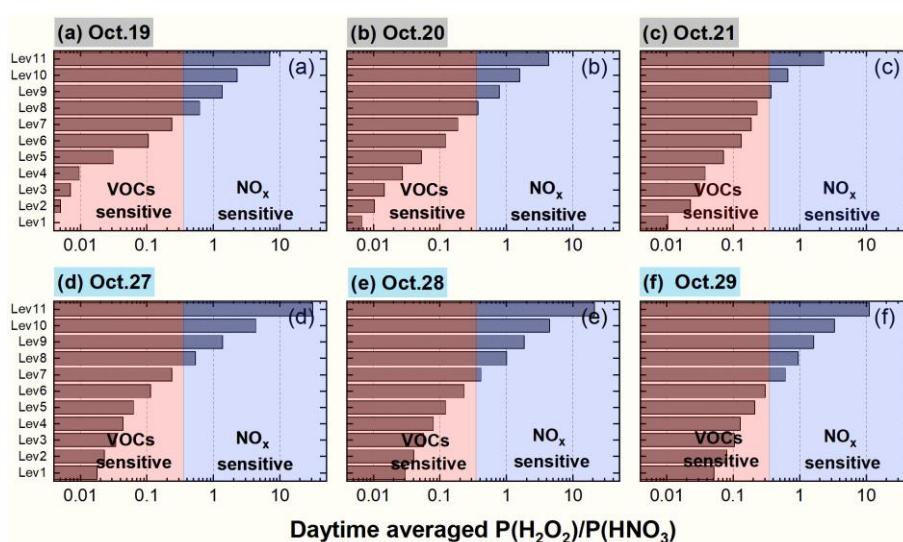
Figure 15 The 95-NCP-site-averaged $P(H_2O_2)/P(HNO_3)$ ratio at each vertical layer for the 6S case

during a typical haze aggravating process of Oct.19–21 (a–c) and a clean period of Oct.27–29 (d–f)

of 2018.

667

668 The specific role of the produced HONO or NO_2 via the $Phot_{nitrate}$ reaction (R2) in

669 DMA8 O_3 enhancements was further analyzed and is shown in **Fig. 16**, the produced

670 NO_2 and HONO jointly promoted O_3 formation and increased DMA8 O_3

671 concentrations. From the surface to ~1200m (Level 9), the DMA8 O_3 enhancements

672 for case D_HONO was ~5 times those for case D_NO$_2$, while at ~2000 m (Level 11)

673 the DMA8 O_3 enhancements for case D_HONO was ~2 times those for case D_NO$_2$.

674 A balance exists between the propagation of the free radical interconversion cycle and

675 the rate of termination of the cycle for the O_3 formation chemistry (Gligorovski et al.,

37

2015), considering the 0.67 and 0.33 yields (ratio is 2) for the two products, we could

conclude that the impact of produced HONO on O_3 enhancements was larger than that

of produced NO_2 near the surface, while at higher altitude (>2000 m) the impacts of

the two products were similar.
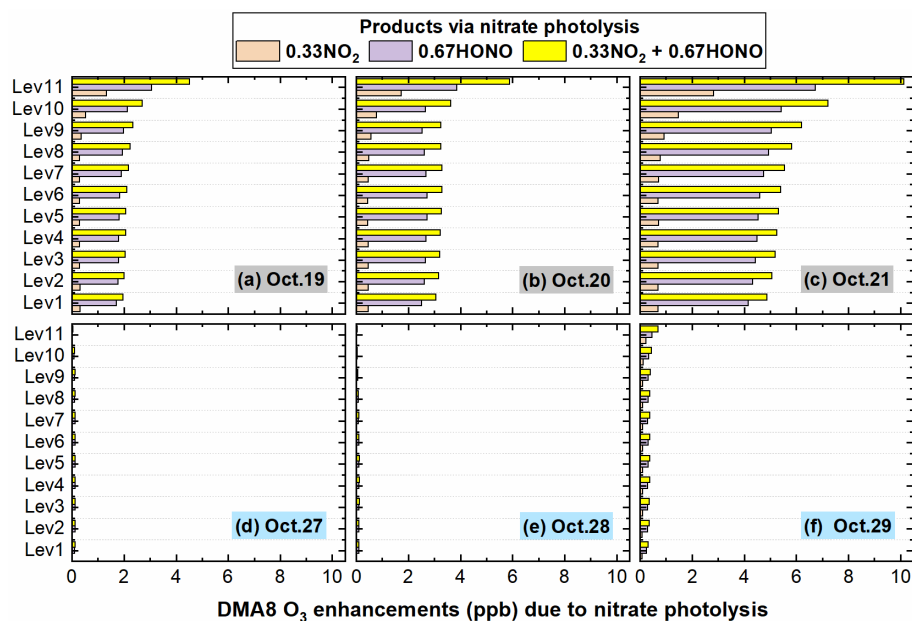
Figure 16 The 95-NCP-site-averaged DMA8 O_3 enhancements due to nitrate photolysis with three

product scenarios (cases D_NO2, D_HONO and D) during a typical haze aggravating process of

Oct.19–21 (a–c) and a clean period of Oct.27–29 (d–f) in 2018.

4. Discussion

4.1 Vertical variations of potential HONO sources

The relative contribution of potential HONO sources near the surface,

corresponding to the first model layer (0 to ~35 m) in our simulation, was quantified

in previous modelling studies (Fu et al., 2019; Xue et al., 2020; Zhang et al., 2021),

however, for those potential HONO sources, their relative contributions to HONO

concentrations near and above the surface should be different. Based on our results

(**Figs.7&8**), the effects of aerosol related HONO sources would be severely

underestimated in hazy days when only focused surface HONO, especially for

$Phot_{nitrate}$. Near the surface in NCP, the daytime contribution of $Phot_{nitrate}$ to HONO

concentrations in hazy days was only ~4–6%, but this source contributed ~35–50% of

the enhanced DMA8 O_3 (**Fig.14a–c**); above the eighth layer (~800 m), this source

contributed ~50–70% of HONO concentrations and ~50–95% of the enhanced DMA8

O_3 (**Fig.14a–c**).

A recent observation in urban Beijing reported vertical HONO concentrations

from three heights above the ground and found that extremely high HONO

concentrations occurred at 120 m (~5 ppb) and 240 m (~3 ppb) rather than near the

surface (~1.2 ppb) during 12:00 in a typical hazy day (Zhang et al., 2020b). The

observation was unusual at noontime under strong convection conditions, inconsistent

with those most previous observations indicating a HONO decrease trend with height,

especially with the observational results of Zhu et al. (2011) and Meng et al. (2020)

and simulated results of Zhang et al. (2021) and ours in **Fig.S6** at the same

observational site. The contributions of different HONO sources at each layer were

analyzed by using a box model, but ~80–90% of the noontime HONO at higher layers

could not be explained by the known HONO formation mechanisms (Zhang et al.,

2019c). The box model neglected the vertical convection, so the ground related

712 HONO sources had no contribution to HONO concentrations at the higher layers, thus

713 their HONO simulations were actually underestimated compared with our results and

714 the previous studies of Wong et al. (2011) and Zhang et al. (2021).

715

4.2 Uncertainties of $J_{nitrate}/J_{HNO3}$ ratios and their impacts

4.2.1 Uncertainties of $J_{nitrate}/J_{HNO3}$ ratios in DMA8 O_3 enhancements

718 Based on our results, Het_{ground} and $Phot_{nitrate}$ were the two major contributors to

719 the enhanced DMA8 O_3, especially for $Phot_{nitrate}$ in hazy days with higher $PM_{2.5}$

720 concentrations. The uncertainties of $Phot_{nitrate}$ (four $J_{nitrate}/J_{HNO3}$ ratios) in O_3

721 enhancements were analyzed and are shown in **Fig.17** (The uncertainties of Het_{ground}

722 are presented in **text S2**). During the haze aggravating process, the enhanced DMA8

723 O_3 near the surface increased from ~0.3 to ~0.5 ppb, from ~0.9 to ~2 ppb, from ~2 to

724 ~6 ppb, and from ~5 to ~12 ppb, with the $J_{nitrate}/J_{HNO3}$ ratio being 1, 7, 30, 120,

725 respectively, and the enhanced O_3 increased with altitude. In clean days, the impact of

726 $Phot_{nitrate}$ on O_3 enhancements was small (<1 ppb) even with a $J_{nitrate}/J_{HNO3}$ ratio of

727 120.

728

729
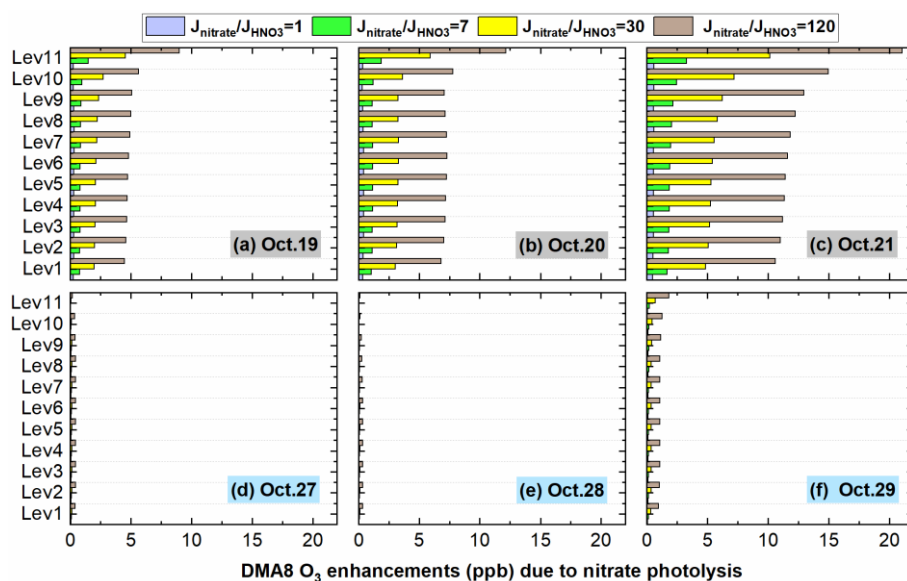
Figure 17 The 95-NCP-site-averaged DMA8 O_3 enhancement induced by nitrate photolysis with

731   four $J_{nitrate}/J_{HNO3}$ ratios (1, 7, 30 and 120) during a typical haze aggravating process of Oct.19–21

732   (a–c) and a clean period of Oct.27–29 (d–f) of 2018.

733

4.2.2 Uncertainties of $J_{nitrate}/J_{HNO3}$ ratios in nitrate concentrations

735   We found considerable enhancements in O_3 concentrations induced by $Phot_{nitrate}$,

736   yet it is still unclear that to what extent $Phot_{nitrate}$ could influence nitrate

737   concentrations. The overall nitrate concentrations for the base case and the nitrate

738   enhancements induced by the potential HONO sources decreased with rising altitude

739   except for $Phot_{nitrate}$ (**Fig.S9a**). Het_{ground} enhanced nitrate concentrations by ~1.5 µg

740   m^{-3} near the surface and the enhancements decreased to < 0.5µg m^{-3} above the eighth

741   model layer (~800m); the nitrate enhancements due to $Het_{aerosol}$ and $E_{traffic}$ near the

742   surface were ~0.2 and ~0.1 µg m^{-3}, respectively, and were < 0.1 and < 0.04 µg m^{-3}

743   above the sixth model layer (~500m). For $Phot_{nitrate}$, the overall impact of four

41

744 $J_{nitrate}/J_{HNO3}$ ratios on nitrate concentrations is shown in **Fig.S9b**, a smaller $J_{nitrate}/J_{HNO3}$

745 ratio of 1 or 7 had a limited impact on nitrate concentrations of ~0–0.05 μg m^{-3}, a

746 $J_{nitrate}/J_{HNO3}$ ratio of 30 slightly decreased nitrate concentrations by ~0.2 μg m^{-3}, while

747 the $J_{nitrate}/J_{HNO3}$ ratio of 120 decreased vertical nitrate concentrations by ~0.3–0.8 μg

748 m^{-3}. The relative nitrate changes caused by Phot$_{nitrate}$ were calculated by the

749 differences between four cases added Phot$_{nitrate}$ (cases Nit_1, Nit_7, D and Nit_120)

750 and the base case (**Fig.S9c**). The vertical nitrate concentrations were reduced by ~0–

751 0.4% ($J_{nitrate}/J_{HNO3}$=1), ~0–2% (7), ~2–5% (30) and ~10–14% (120) at the 95 NCP

752 sites, meaning that the Phot$_{nitrate}$ impact on vertical nitrate concentrations is limited

753 (<5%) when adopting a relatively small $J_{nitrate}/J_{HNO3}$ ratio (< 30) (**Fig.S9c**).

754 Romer et al. (2018) found a $J_{nitrate}/J_{HNO3}$ ratio of 10 or 30 had a much larger effect

755 on HONO than on HNO$_3$, and Phot$_{nitrate}$ accounted for an average of 40% of the total

756 production of HONO, and only 10% of HNO$_3$ loss with a $J_{nitrate}/J_{HNO3}$ ratio of 10

757 (Fig.5 in Romer et al. (2018)), consistent with our study. From the production rate of

758 gas HNO$_3$ (P$_{HNO3}$) in **Fig.S10**, we can find that an increase in the $J_{nitrate}/J_{HNO3}$ ratio for

759 Phot$_{nitrate}$ simultaneously enhances the HNO$_3$ production rate, and is favorable for

760 nitrate formation via the reaction between HNO$_3$ and NH$_3$. Nitrate consumption is

761 mitigated by the faster nitrate formation, this is the main reason for less perturbation

762 of the nitrate budget influenced by Phot$_{nitrate}$.

763 **Fig.18** shows the detailed relative changes of nitrate caused by Phot$_{nitrate}$ during a

764 typical haze aggravating process and a clean period (corresponding concentrations are

765 shown in **Fig.S11**). The percentage nitrate reduction was usually smaller in hazy days

than in clean days, mainly due to the slightly weaker photolysis frequency in pollution

events (**Fig.S7**). The nitrate reduction was <5% when adopting a $J_{nitrate}/J_{HNO_3}$ ratio of

30 in both clean and hazy days and was <15% in most cases even when the

$J_{nitrate}/J_{HNO_3}$ ratio reached 120.
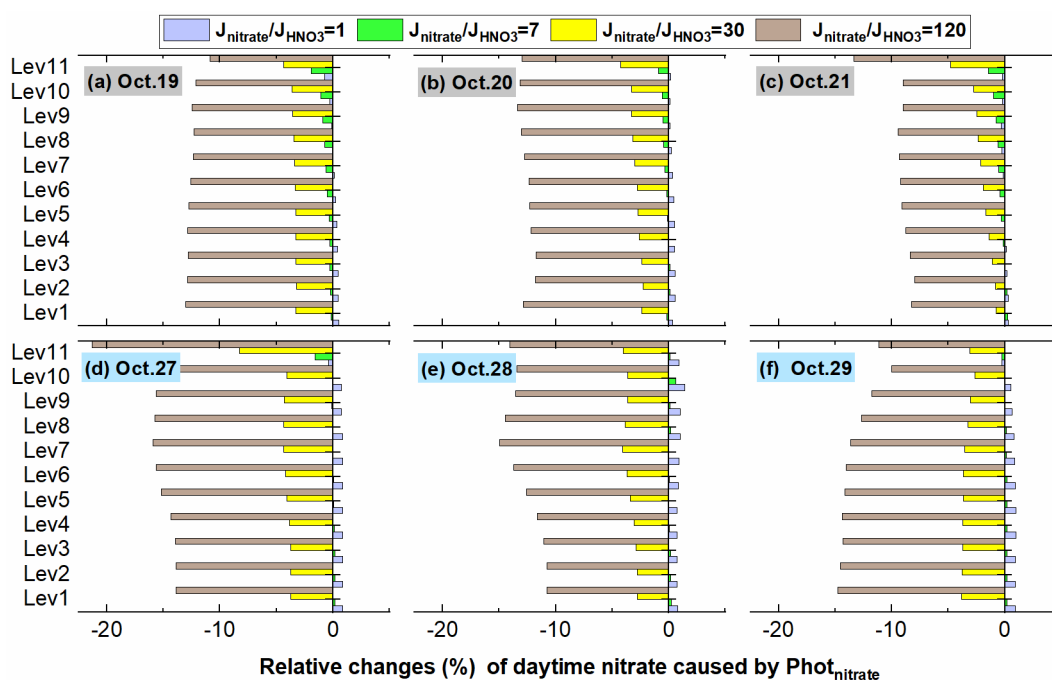
Figure 18 The 95-NCP-site-averaged relative changes of nitrate with four $J_{nitrate}/J_{HNO_3}$ ratios (1, 7,

30 and 120) compared with the base case during a typical haze aggravating process of Oct.19–21

(a–c) and a clean period of Oct.27–29 (d–f) of 2018.

4.2.3 Possible ranges of the $J_{nitrate}/J_{HNO_3}$ ratio

From the above discussion, we can find that the enhanced OH and O_3 due to

$Phot_{nitrate}$ are remarkable during haze aggravating processes, and the exact value of the

$J_{nitrate}/J_{HNO_3}$ ratio requires more studies.

780   **Fig. 19** shows diurnal patterns of surface-averaged and vertically-averaged

781 simulations of the $Phot_{nitrate}$ frequency with four different $J_{nitrate}/J_{HNO3}$ ratios at the 95

782 NCP sites during the study period. The $Phot_{nitrate}$ frequency at 12:00 was 3.7×10^{-7},

783 2.6×10^{-6}, 1.1×10^{-5} and 4.5×10^{-5} s^{-1}, when adopting a $J_{nitrate}/J_{HNO3}$ ratio of 1, 7, 30 and

784 120, respectively. The corresponding vertically-averaged $Phot_{nitrate}$ frequency was

785 slightly larger (~10%) and was 4.2×10^{-7}, 2.9×10^{-6}, 1.3×10^{-5} and 5.0×10^{-5} s^{-1},

786 respectively. Adopting a $J_{nitrate}/J_{HNO3}$ ratio of 30 in the 6S case, with the corresponding

787 $J_{nitrate}$ of $1.1–1.3\times10^{-5}$ s^{-1}, produced ~30–50% of the enhanced O_3 near the surface in

788 hazy days (**Fig.13**), and ~70–90% of the enhanced O_3 at higher layers (>800 m).

789   The reported values of $J_{nitrate}$ from previous studies are summarized in **Table 4**.

790 The experimental $J_{nitrate}$ values have been controversial over the past two decades and

791 are still arguable currently. In our simulations for the 6S case, $Phot_{nitrate}$ contributed

792 from ~1% (clean days) to ~5% (hazy days) to surface HONO during daytime when

793 using the $J_{nitrate}/J_{HNO3}$ ratio of 30 in NCP, consistent with <8% at a rural site in NCP

794 reported by Xue et al. (2020) and ~1% at urban Beijing reported by Zhang et al. (2021)

795 using the same ratio; however, the increasing contribution of $Phot_{nitrate}$ to HONO

796 concentrations with rising altitude based on our simulations (**Fig.7**), has not been

797 discussed in previous research. Furthermore, we found that the overall $Phot_{nitrate}$

798 impact to OH and O_3 would be severely underestimated when the $Phot_{nitrate}$

799 contribution to vertical HONO was excluded.

800   A larger $J_{nitrate}/J_{HNO3}$ ratio of 120 for $Phot_{nitrate}$ ($4.5–5.0\times10^{-5}$ s^{-1} at 12:00) produced

801 ~25–30% of noontime HONO in NCP in our study (**Fig.S12**), comparable with 30–40%

802 in previous modelling studies (Fu et al., 2019; Shi et al., 2020) when using the

803 $J_{nitrate}/J_{HNO3}$ ratio of 118.57 ($8.3\times10^{-5}/ 7\times10^{-7}$). In haze aggravating processes, the

804 contribution of Phot$_{nitrate}$ ($J_{nitrate}/J_{HNO3}$ = 120) to the DMA8 O_3 enhancements reached

805 ~5–10 ppb near the surface and ~8–20 ppb above the tenth model layer (**Fig.17**), these

806 enhancements were extremely large. In a previous modelling study by Fu et al. (2020),

807 the daytime surface O_3 simulations were systematically overestimated by ~ 5 ppb in

808 NCP in winter (**Fig.S4** in Fu et al. (2020)), the inclusion of Phot$_{nitrate}$ ($J_{nitrate}/J_{HNO3}$ =

809 118.57) in their study might cause the overestimation. From the above, a $J_{nitrate}/J_{HNO3}$

810 ratio of 120, or a $J_{nitrate}$ value of ~4–5$\times10^{-5}$ s^{-1} is possibly overestimated. When

811 adopting the maximum $J_{nitrate}$ value of 10^{-4} s^{-1} reported by Ye et al. (2016a) and Bao et

812 al. (2018), we reasonably speculate that O_3 simulations will be significantly

813 overestimated, especially at higher altitude with NO_x-sensitive O_3 chemistry (**Fig.15**).

814   Romer et al. (2018) and Kasibhatla et al. (2018) suggested that a $J_{nitrate}/J_{HNO3}$ ratio

815 of 30 or smaller would be more suitable, being about the minimum value reported by

816 Ye et al. (2016a) and Bao et al. (2018), this ratio has shown significant influence on

817 the O_3 simulations in haze aggravating processes in this study. The lack of

818 photo-catalyzer in suspended submicron particulate sodium and ammonium nitrate

819 may cause a lower $J_{nitrate}/J_{HNO3}$ ratio (<10) reported by Shi et al. (2021), so more

820 chamber experiments need to be conducted by using the particles collected in the real

821 atmosphere. Choosing a larger $J_{nitrate}$ value might cover up other ground-based

822 unknown HONO sources, creating an illusion of good model simulations of daytime

823 HONO, but resulting in overestimation of O_3 concentrations. Considering the

824 uncertainties of NO_x or VOCs emissions, which also significantly impact O_3

825 simulations, more studies are needed to find the exact value of $J_{nitrate}$ in the real

826 atmosphere.

827
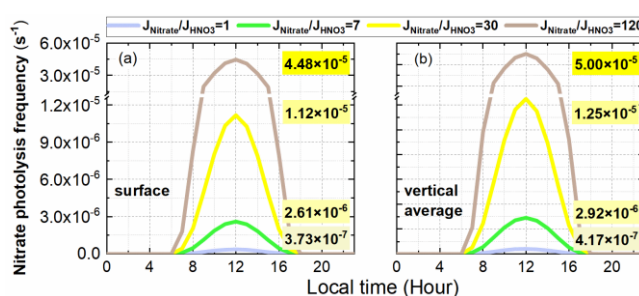
828

829 **Figure 19** Diurnal patterns of surface-averaged (a) and vertically-averaged (b) simulations of the

830 nitrate photolysis frequency with four different $J_{nitrate}$/J_{HNO3} ratios (1, 7, 30, 120) at the 95 NCP

831 sites during the study period (The nitrate photolysis frequencies at 12:00 are shown in each graph).

832
833
834

835 **Table 4.** Summary of studies on the nitrate photolysis frequency ($J_{nitrate}$) (J_{HNO3} denotes the photolysis
836 frequency of gas HNO_3)

Experimental conditions	Main conclusion	Reference
HNO_3 absorbed on Pyrex surface	$J_{nitrate}$ (1.2×10^{-5} s^{-1}) is 1–2 orders of magnitude faster than in the gas and aqueous phases.	(Zhou et al., 2003)
Atmosphere simulation chamber	$J_{nitrate}$ on snow, ground, and glass surfaces, can be excluded in the chamber.	(Rohrer et al., 2005)
HNO_3 absorbed on glass surface	Photolysis frequency of surfaces adsorbed HNO_3 is > 2 orders of magnitude larger than J_{HNO3}.	(Zhu et al., 2008)
Urban grime-coated surface	$J_{nitrate}$ (1.2×10^{-3} s^{-1}) is 4 orders of magnitude faster than in water (10^{-7} s^{-1}).	(Baergen and Donaldson, 2013)
Various natural/artificial surfaces	$J_{nitrate}$ ranges from 6.0×10^{-6} s^{-1} to 3.7×10^{-4} s^{-1}, 1–3 orders of magnitude higher than J_{HNO3}	(Ye et al., 2016a)
Adsorbed HNO_3 on glass surfaces	Photolysis frequency of surfaces adsorbed HNO_3 (2.4×10^{-7} s^{-1}) is very low.	(Laufs and Kleffmann, 2016)

Aerosol filter samples	$J_{nitrate}$ ranges from 6.2×10^{-6} s^{-1} to 5.0×10^{-4} s^{-1} with a mean of 1.3×10^{-4} s^{-1}.	(Ye et al., 2017)
Nitrate aerosol in the MBL	$J_{nitrate}$ is ~10 times higher than J_{HNO3}.	(Reed et al., 2017)
PM$_{2.5}$ in Beijing	$J_{nitrate}$ (1.22×10^{-5} s^{-1} to 4.84×10^{-4} s^{-1}) is 1–3 orders of magnitude higher than J_{HNO3}.	(Bao et al., 2018)
Sea-salt particulate nitrate	$J_{nitrate}$ is 25–50 times higher than J_{HNO3}.	(Kasibhatla et al., 2018)
Particles collected on filters	$J_{nitrate}$ is $\leq$ 30 times J_{HNO3}.	(Romer et al., 2018)
CMAQ simulation	Nitrate photolysis contributed ~30% of noontime HONO with a $J_{nitrate}/J_{HNO3}$ ratio of ~120.	(Fu et al., 2019)
CMAQ simulation	A $J_{nitrate}/J_{HNO3}$ ratio of 100 better improved sulfate simulations than a $J_{nitrate}/J_{HNO3}$ ratio of 10.	(Zheng et al., 2020)
MCM Box model	Nitrate photolysis contribution to HONO was < 8% with a $J_{nitrate}/J_{HNO3}$ ratio of 30.	(Xue et al., 2020)
MCM Box model	Nitrate photolysis contributed ~40% of noontime HONO with a $J_{nitrate}/J_{HNO3}$ ratio of ~120.	(Shi et al., 2020)
Smog chamber	The $J_{nitrate}/J_{HNO3}$ ratio was <10 for suspended submicron $NaNO_3$ and NH_4NO_3.	(Shi et al., 2021)
CMAQ simulation	Nitrate photolysis contribution to surface HONO was ~1.0% with a $J_{nitrate}/J_{HNO3}$ ratio of 30.	(Zhang et al., 2021)
WRF-Chem simulation	The relative contribution of nitrate photolysis to HONO increased with rising altitude and nitrate photolysis contributed much larger in the ABL than near the surfaceto the enhanced O_3. On average, nitrate photolysis contributed ~5% of surface daytime HONO with a $J_{nitrate}/J_{HNO3}$ ratio of 30 (~1×10^{-5} s^{-1}) but contributed ~30–50% of the enhanced O_3 near the surface in NCP in hazy days.	This study

837   MBL: marine boundary layer; ABL: atmospheric boundary layer.
838

4.3 Interactions between heterogeneous HONO sources

840   Form the comparison of nitrate budget induced by the six potential HONO

841   sources in **Fig.S3&S9**, we can find that Het$_{ground}$ led to an significant increase in

842   nitrate concentrations. In the real atmosphere, the NO$_2$ heterogeneous reactions and

843   the Phot$_{nitrate}$ reaction occur simultaneously, while the sensitivity tests only considered

844   one specific HONO source for each case and neglected their interactions, leading to

845   the underestimation of the Phot$_{nitrate}$ impact to some extent. Take it into consideration,

846   the Phot$_{nitrate}$ impact on atmospheric oxidants and secondary pollutants would be even

847   larger, especially during the haze aggravating process.

848   Phot$_{nitrate}$ would in turn change NO$_x$ concentrations to some extent. From the

849   95-site-averaged NO$_2$ concentrations shown in **Fig. 20**, we can find that Phot$_{nitrate}$

850   slightly increased NO$_2$ concentrations in hazy days. The elevated NO$_2$ concentration

851   could enhance HONO formation via the NO$_2$ heterogeneous reactions, nevertheless,

852   due to the high background NO$_2$ concentrations in NCP (up to ~ 40 ppb at nighttime),

853   the increment of NO$_2$ and the enhanced HONO formation from NO$_2$ caused by

854   Phot$_{nitrate}$ were small (<10%), but might have a larger impact on NO$_x$ budgets in clean

855   regions. From the above, a positive feedback relationship between the NO$_2$

856   heterogeneous reactions and the Phot$_{nitrate}$ reaction could be found, these

857   multi-processes worse the air quality during the haze aggravating processes.
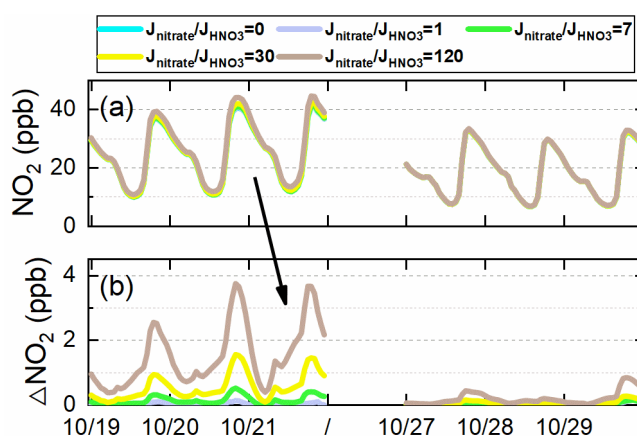
858

859   **Figure 20** Comparison of 95-site-averaged simulations of NO$_2$ concentrations for the base case and

860   four cases with different J$_{nitrate}$/J$_{HNO3}$ ratios (1, 7, 30 and 120) (a), and the corresponding NO$_2$ variations

861   (b) compared with the base case in the North China Plain during Oct.11–31 of 2018.

862

5. Conclusions

In this study, three direct emission sources, the improved NO_2 heterogeneous reactions on aerosol and ground surfaces, and particulate nitrate photolysis in the atmosphere were included into the WRF-Chem model to explore the key HONO sources producing O_3 enhancements during typical autumn haze aggravating processes with co-occurrence of high $PM_{2.5}$ and O_3 in NCP. The six potential HONO sources produced a significant enhancement in surface HONO simulations and improved the mean HONO concentration at the BUCT site to 1.47 ppb from 0.05 ppb (improved the NMB to -14.22% from -97.11% and the IOA to 0.80 from 0.45). The improved HONO significantly enhanced the atmospheric oxidation capacity near the surface and at elevated heights, especially in hazy days, resulting in fast formation of and significant improvements of O_3 during haze aggravating processes in NCP. Although the photolysis frequency is usually lower during hazy days, higher concentrations of NO_2, $PM_{2.5}$ and nitrate favored HONO formation via heterogeneous reactions, leading to stronger atmospheric oxidation capacity. The major results include:

(1) For the surface HONO in NCP, Het_{ground} was the largest source during daytime and nighttime (~50–80%); the contribution of $Phot_{nitrate}$ ($J_{nitrate}/J_{HNO3} = 30$) to surface HONO concentrations was close to that of the NO+OH reaction during daytime (~1–12%) and was ~5% for daytime average; $E_{traffic}$ was important during nighttime (~10–20%) but small during daytime (<5%); the contribution of $Het_{aerosol}$ was minor (~2–3%) in daytime and <10% in nighttime; the contribution of E_{soil} was

885　<3%, and E_{indoor} could be neglected. Vertically, the HONO enhancements due to

886　ground-based potential HONO sources ($E_{traffic}$, E_{soil}, E_{indoor} and Het_{ground}) decreased

887　rapidly with height, while the NO+OH reaction and aerosol-related HONO sources

888　($Phot_{nitrate}$ and $Het_{aerosol}$) decreased with height much slower. The enhanced HONO

889　due to $Phot_{nitrate}$ in hazy days was about ten times larger than in clean days and

890　became the dominant HONO source (~30–70% when $J_{nitrate}/J_{HNO3}$ = 30) at higher

891　layers, and both HONO concentrations and $Phot_{nitrate}$ contributions increased with the

892　aggravated pollution levels.

893　　(2) Near the surface, daytime OH production/loss rates were significantly

894　enhanced by~320% for the 6S case (mean was 5.27 ppb h^{-1}) compared with the base

895　case (mean was 1.26 ppb h^{-1}); vertically, daytime OH production/loss rates were

896　enhanced by ~105% for the 6S case (mean was 2.21 ppb h^{-1}) compared with the base

897　case (mean was 1.08 ppb h^{-1}). The enhanced OH production rate and OH due to the

898　six potential HONO sources both showed a strong positive correlation with $PM_{2.5}$

899　concentrations at the 95 NCP sites, with a slope of 0.043 ppb h^{-1}/µg m^{-3} of $PM_{2.5}$ and

900　3.62×10^4 molec cm^{-3}/µg m^{-3} of $PM_{2.5}$ from the surface to the height of 2.5 km for case

901　6S, respectively. The atmospheric oxidation capacity (e.g., OH) was enhanced in the

902　haze aggravating process.

903　　(3) A strong positive correlation (r>0.8) between enhanced O_3 by the six potential

904　HONO sources and $PM_{2.5}$ concentrations was found in NCP, and nitrate photolysis

905　was the largest contributor to the enhanced DMA8 O_3 in hazy days. Vertically, the

906　enhanced DMA8 O_3 was < 2ppb when $PM_{2.5}$ was < 20µg m^{-3}, and that was >10 ppb

51

907   when $PM_{2.5}$ was > 60μg m^{-3} on average, with a slope of 0.24 ppb DMA8 O_3

908   enhancement /μg m^{-3} of $PM_{2.5}$. The surface enhanced DMA8 O_3 was ~5.5 ppb

909   (Oct.19), ~7 ppb (Oct.20) and ~10 ppb (Oct.21), respectively, during a typical haze

910   aggravating process, while that was usually ~2 ppb in clean days. The contribution of

911    $Phot_{nitrate}$ to the enhanced DMA8 O_3 was increased by over one magnitude during the

912   haze aggravating process (up to 5–10 ppb) compared with that in clean days (~0.1–0.5

913   ppb), reached ~2–4.5 ppb (Oct.19), ~3–6 ppb (Oct.20) and ~5–10 ppb (Oct.21),

914   respectively, during a typical haze aggravating process vertically.

915   (4) Surface O_3 was controlled by VOCs-sensitive chemistry, while O_3 at higher

916   altitude (>800m) was controlled by NO_x-sensitive chemistry in NCP during autumn.

917   The nitrate photolysis reaction enhanced OH and NO_x concentrations, both favored O_3

918   formation at high altitude, especially in haze aggravating processes with abundant

919   nitrate. The produced HONO rather than the produced NO_2 through nitrate photolysis

920   had a stronger promotion for O_3 formation near the surface, but the impacts of the two

921   products on O_3 enhancements were similar at higher altitude (~2000 m).

922   (5) Nitrate photolysis only contributed ~5% of the surface HONO in daytime

923   with a $J_{nitrate}$/J_{HNO3} ratio of 30 (~1×10^{-5} s^{-1}) but contributed ~30–50% of the enhanced

924   O_3 near the surface in NCP in hazy days. The photolysis of nitrate had a limited

925   impact on nitrate concentrations (reduced by <5% with $J_{nitrate}$/J_{HNO3} =30, and <15%

926   even with a $J_{nitrate}$/J_{HNO3} ratio of 120), due mainly to the simultaneously enhanced

927   atmospheric oxidants favoring the formation of HNO_3 and nitrate. Choosing a larger

928    $J_{nitrate}$ value might cover up other ground-based unknown HONO sources, but

929 overestimate vertical sources of HONO, and NO_x and O_3 concentrations, so more

930 studies are still needed to find the exact value of $J_{nitrate}$ in the real atmosphere.

931

Data availability

933 Data are available upon reasonable request to the corresponding authors.

934

Author contribution:

936 J.Z., C.L., J.A., M.G., and W.W. conceived and designed the research. J.Z. performed

937 WRF-Chem simulations and wrote the paper. J.Z., C.L., Y.G., and H.R. performed

938 data analyses and produced the figures. C.L., Y.Z., F.Z., X.F., C.Y., K.D., Y.L., and

939 M.K. conducted the field observations. W.W., J.A., M.G., Y.L., and M.K. reviewed the

940 article.

Competing interests

942 The authors declare that they have no conflict of interest.

943

Acknowledgements

950

References

Alicke, B., Platt, U., Stutz, J., 2002. Impact of nitrous acid photolysis on the total hydroxyl radical budget during the Limitation of Oxidant Production/Pianura Padana Produzione di Ozono study in Milan. J Geophys Res-Atmos 107. doi:10.1029/2000JD000075.

An, J.L., Li, Y., Chen, Y., Li, J., Qu, Y., Tang, Y.J., 2013. Enhancements of major aerosol components due to additional HONO sources in the North China Plain and implications for visibility and haze. Advances in Atmospheric Sciences 30, 57-66.

Aumont, B., Chervier, F., Laval, S., 2003. Contribution of HONO sources to the $NO_x/HO_x/O_3$ chemistry in the polluted boundary layer. Atmospheric Environment 37, 487-498.

Avnery, S., Mauzerall, D.L., Liu, J., Horowitz, L.W., 2011a. Global crop yield reductions due to surface ozone exposure: 1. Year 2000 crop production losses and economic damage. Atmospheric Environment 45, 2284-2296.

Avnery, S., Mauzerall, D.L., Liu, J., Horowitz, L.W., 2011b. Global crop yield reductions due to surface ozone exposure: 2. Year 2030 potential crop production losses and economic damage under two scenarios of O_3 pollution. Atmospheric Environment 45, 2297-2309.

Baergen, A.M., Donaldson, D.J., 2013. Photochemical renoxification of nitric acid on real urban grime. Environmental Science & Technology 47, 815-820.

Bao, F., Li, M., Zhang, Y., Chen, C., Zhao, J., 2018. Photochemical Aging of Beijing Urban $PM_{2.5}$: HONO Production. Environmental Science & Technology 52, 6309-6316.

Bao, F.X., Jiang, H.Y., Zhang, Y., Li, M., Ye, C.X., Wang, W.G., Ge, M.F., Chen, C.C., Zhao, J.C., 2020. The Key Role of Sulfate in the Photochemical Renoxification on Real $PM_{2.5}$. Environmental Science & Technology 54, 3121-3128.

Bejan, I., Abd-el-Aal, Y., Barnes, I., Benter, T., Bohn, B., Wiesen, P., Kleffmann, J., 2006. The photolysis of ortho-nitrophenols: a new gas phase source of HONO. Physical chemistry chemical physics : PCCP 8, 2028-2035.

Chen, S., Wang, H., Lu, K., Zeng, L., Hu, M., Zhang, Y., 2020a. The trend of surface ozone in Beijing from 2013 to 2019: Indications of the persisting strong atmospheric oxidation capacity. Atmospheric Environment 242, 117801.

Chen, Y., Wang, W.G., Lian, C.F., Peng, C., Zhang, W.Y., Li, J.L., Liu, M.Y., Shi, B., Wang, X.F., Ge, M.F., 2020b. Evaluation and impact factors of indoor and outdoor gas-phase nitrous acid under different environmental conditions. Journal of Environmental Sciences 95, 165-171.

Chen, Y., Zheng, P., Wang, Z., Pu, W., Tan, Y., Yu, C., Xia, M., Wang, W., Guo, J., Huang, D., Yan, C., Nie, W., Ling, Z., Chen, Q., Lee, S., Wang, T., 2021. Secondary Formation and Impacts of Gaseous Nitro-Phenolic Compounds in the Continental Outflow Observed at a Background Site in South China. Environmental Science & Technology. DOI: 10.1021/acs.est.1c04596.

Crowley, J.N., Carl, S.A., 1997. OH formation in the photoexcitation of NO2 beyond the dissociation threshold in the presence of water vapor. Journal of Physical Chemistry A 101, 4178-4184.

Cui, L., Li, R., Fu, H., Meng, Y., Zhao, Y., Li, Q., Chen, J., 2021. Nitrous acid emission from open burning of major crop residues in mainland China. Atmospheric Environment 244, 117950.

Dillon, T.J., Crowley, J.N., 2018. Reactive quenching of electronically excited NO_2^* and NO_3^* by H_2O as potential sources of atmospheric HO_x radicals. Atmospheric Chemistry and Physics 18, 14005-14015.

993 Dong, W., Xing, J., Wang, S., 2010. Temporal and spatial distribution of anthropogenic ammonia
994   emissions in China: 1994-2006. Environmental Sciences (in Chinese) 31, 1457-1463.

995 Emmons, L.K., Walters, S., Hess, P.G., Lamarque, J.F., Pfister, G.G., Fillmore, D., Granier, C.,
996   Guenther, A., Kinnison, D., Laepple, T., Orlando, J., Tie, X., Tyndall, G., Wiedinmyer, C.,
997   Baughcum, S.L., Kloster, S., 2010. Description and evaluation of the Model for Ozone and
998   Related chemical Tracers, version 4 (MOZART-4). Geoscientific Model Development 3, 43-67.

999 Feng, T., Zhao, S., Bei, N., Liu, S., Li, G., 2021. Increasing atmospheric oxidizing capacity weakens
1000   emission mitigation effort in Beijing during autumn haze events. Chemosphere 281, 130855.

1001 Feng, Z., De Marco, A., Anav, A., Gualtieri, M., Sicard, P., Tian, H., Fornasier, F., Tao, F., Guo, A.,
1002   Paoletti, E., 2019. Economic losses due to ozone impacts on human health, forest productivity and
1003   crop yield across China. Environ Int 131, 104966.

1004 Feng, Z., Hu, E., Wang, X., Jiang, L., Liu, X., 2015. Ground-level O_3 pollution and its impacts on food
1005   crops in China: a review. Environ Pollut 199, 42-48.

1006 Feng, Z., Xu, Y., Kobayashi, K., Dai, L., Zhang, T., Agathokleous, E., Calatayud, V., Paoletti, E.,
1007   Mukherjee, A., Agrawal, M., Park, R.J., Oak, Y.J., Yue, X., 2022. Ozone pollution threatens the
1008   production of major staple crops in East Asia. Nature Food 3, 47-56.

1009 Finlayson-Pitts, B.J., Wingen, L.M., Sumner, A.L., Syomin, D., Ramazan, K.A., 2003. The
1010   heterogeneous hydrolysis of NO_2 in laboratory systems and in outdoor and indoor atmospheres:
1011   An integrated mechanism. Physical Chemistry Chemical Physics 5, 223-242.

1012 Fröhlich, R., Cubison, M.J., Slowik, J.G., Bukowiecki, N., Prévôt, A.S.H., Baltensperger, U., Schneider,
1013   J., Kimmel, J.R., Gonin, M., Rohner, U., Worsnop, D.R., Jayne, J.T., 2013. The ToF-ACSM: a
1014   portable aerosol chemical speciation monitor with TOFMS detection. Atmospheric Measurement
1015   Techniques 6, 3225-3241.

1016 Fu, X., Wang, T., Gao, J., Wang, P., Liu, Y.M., Wang, S.X., Zhao, B., Xue, L.K., 2020. Persistent Heavy
1017   Winter Nitrate Pollution Driven by Increased Photochemical Oxidants in Northern China.
1018   Environmental Science & Technology 54, 3881-3889.

1019 Fu, X., Wang, T., Zhang, L., Li, Q.Y., Wang, Z., Xia, M., Yun, H., Wang, W.H., Yu, C., Yue, D.L., Zhou,
1020   Y., Zheng, J.Y., Han, R., 2019. The significant contribution of HONO to secondary pollutants
1021   during a severe winter pollution event in southern China. Atmospheric Chemistry and Physics 19,
1022   1-14.

1023 Gao, W., Tan, G., Hong, Y., Li, M., Nian, H., Guo, C., Huang, Z., Fu, Z., Dong, J., Xu, X., 2013.
1024   Development of portable single photon ionization time-of-flight mass spectrometer combined with
1025   membrane inlet. International Journal of Mass Spectrometry 334, 8-12.

1026 Ge, M., Tong, S., Wang, W., Zhang, W., Chen, M., Peng, C., Li, J., Zhou, L., Chen, Y., Liu, M., 2021.
1027   Important Oxidants and Their Impact on the Environmental Effects of Aerosols. The journal of
1028   physical chemistry. A.125, 3813-3825.

1029 Ge, S., Wang, G., Zhang, S., Li, D., Xie, Y., Wu, C., Yuan, Q., Chen, J., Zhang, H., 2019. Abundant
1030 NH_3 in China Enhances Atmospheric HONO Production by Promoting the Heterogeneous
1031   Reaction of SO_2 with NO_2. Environmental Science & Technology 53, 14339-14347.

1032 Gen, M., Liang, Z., Zhang, R., Go Mabato, B.R., Chan, C.K., 2022. Particulate nitrate photolysis in the
1033   atmosphere. Environmental Science: Atmospheres. DOI: 10.1039/D1EA00087J.

1034 Gligorovski, S., Strekowski, R., Barbati, S., Vione, D., 2015. Environmental Implications of Hydroxyl
1035   Radicals (*OH). Chem Rev 115, 13051-13092.

1036 Gómez Alvarez, E., Sörgel, M., Gligorovski, S., Bassil, S., Bartolomei, V., Coulomb, B., Zetzsch, C.,

Wortham, H., 2014. Light-induced nitrous acid (HONO) production from NO_2 heterogeneous reactions on household chemicals. Atmospheric Environment 95, 391-399.

Guenther, A.B., Jiang, X., Heald, C.L., Sakulyanontvittaya, T., Duhl, T., Emmons, L.K., Wang, X., 2012. The Model of Emissions of Gases and Aerosols from Nature version 2.1 (MEGAN2.1): an extended and updated framework for modeling biogenic emissions. Geoscientific Model Development 5, 1471-1492.

Guo, Y., Zhang, J., An, J., Qu, Y., Liu, X., Sun, Y., Chen, Y., 2020. Effect of vertical parameterization of a missing daytime source of HONO on concentrations of HONO, O_3 and secondary organic aerosols in eastern China. Atmospheric Environment 226, 117208.

Hendrick, F., Muller, J.F., Clemer, K., Wang, P., De Maziere, M., Fayt, C., Gielen, C., Hermans, C., Ma, J.Z., Pinardi, G., Stavrakou, T., Vlemmix, T., Van Roozendael, M., 2014. Four years of ground-based MAX-DOAS observations of HONO and NO_2 in the Beijing area. Atmospheric Chemistry and Physics 14, 765-781.

Huang, X., Li, M.M., Li, J.F., Song, Y., 2012. A high-resolution emission inventory of crop burning in fields in China based on MODIS Thermal Anomalies/Fire products. Atmospheric Environment 50, 9-15.

Kasibhatla, P., Sherwen, T., Evans, M.J., Carpenter, L.J., Reed, C., Alexander, B., Chen, Q.J., Sulprizio, M.P., Lee, J.D., Read, K.A., Bloss, W., Crilley, L.R., Keene, W.C., Pszenny, A.A.P., Hodzic, A., 2018. Global impact of nitrate photolysis in sea-salt aerosol on NO_x, OH, and O_3 in the marine boundary layer. Atmospheric Chemistry and Physics 18, 11185-11203.

Kim, S., VandenBoer, T.C., Young, C.J., Riedel, T.P., Thornton, J.A., Swarthout, B., Sive, B., Lerner, B., Gilman, J.B., Warneke, C., Roberts, J.M., Guenther, A., Wagner, N.L., Dube, W.P., Williams, E., Brown, S.S., 2014. The primary and recycling sources of OH during the NACHTT-2011 campaign: HONO as an important OH primary source in the wintertime. J Geophys Res-Atmos 119, 6886-6896.

Kleffmann, J., Kurtenbach, R., Lorzer, J., Wiesen, P., Kalthoff, N., Vogel, B., Vogel, H., 2003. Measured and simulated vertical profiles of nitrous acid - Part I: Field measurements. Atmospheric Environment 37, 2949-2955.

Klosterkother, A., Kurtenbach, R., Wiesen, P., Kleffmann, J., 2021. Determination of the emission indices for NO, NO_2, HONO, HCHO, CO, and particles emitted from candles. Indoor Air 31, 116-127.

Kramer, L.J., Crilley, L.R., Adams, T.J., Ball, S.M., Pope, F.D., Bloss, W.J., 2020. Nitrous acid (HONO) emissions under real-world driving conditions from vehicles in a UK road tunnel. Atmospheric Chemistry and Physics 20, 5231-5248.

Kubota, M., Asami, T., 1985. Volatilization of Nitrous-Acid from Upland Soils. Soil Science and Plant Nutrition 31, 27-34.

Kurtenbach, R., Becker, K.H., Gomes, J.A.G., Kleffmann, J., Lorzer, J.C., Spittler, M., Wiesen, P., Ackermann, R., Geyer, A., Platt, U., 2001. Investigations of emissions and heterogeneous formation of HONO in a road traffic tunnel. Atmospheric Environment 35, 3385-3394.

Laufs, S., Kleffmann, J., 2016. Investigations on HONO formation from photolysis of adsorbed HNO_3 on quartz glass surfaces. Physical Chemistry Chemical Physics 18, 9616-9625.

Lee, J.D., Whalley, L.K., Heard, D.E., Stone, D., Dunmore, R.E., Hamilton, J.F., Young, D.E., Allan, J.D., Laufs, S., Kleffmann, J., 2016. Detailed budget analysis of HONO in central London reveals a missing daytime source. Atmospheric Chemistry and Physics 16, 2747-2764.

Li, G., Lei, W., Zavala, M., Volkamer, R., Dusanter, S., Stevens, P., Molina, L.T., 2010. Impacts of HONO sources on the photochemistry in Mexico City during the MCMA-2006/MILAGO Campaign. Atmospheric Chemistry and Physics 10, 6551-6567.

Li, K., Jacob, D.J., Shen, L., Lu, X., De Smedt, I., Liao, H., 2020. Increases in surface ozone pollution in China from 2013 to 2019: anthropogenic and meteorological influences. Atmospheric Chemistry and Physics 20, 11423-11433.

Li, L., Chen, C.H., Huang, C., Huang, H.Y., Zhang, G.F., Wang, Y.J., Wang, H.L., Lou, S.R., Qiao, L.P., Zhou, M., Chen, M.H., Chen, Y.R., Streets, D.G., Fu, J.S., Jang, C.J., 2012. Process analysis of regional ozone formation over the Yangtze River Delta, China using the Community Multi-scale Air Quality modeling system. Atmospheric Chemistry and Physics 12, 10971-10987.

Li, M., Zhang, Q., Kurokawa, J., Woo, J.H., He, K.B., Lu, Z.F., Ohara, T., Song, Y., Streets, D.G., Carmichael, G.R., Cheng, Y.F., Hong, C.P., Huo, H., Jiang, X.J., Kang, S.C., Liu, F., Su, H., Zheng, B., 2017. MIX: a mosaic Asian anthropogenic emission inventory under the international collaboration framework of the MICS-Asia and HTAP. Atmospheric Chemistry and Physics 17, 935-963.

Li, S., Matthews, J., Sinha, A., 2008. Atmospheric hydroxyl radical production from electronically excited NO_2 and H_2O. Science 319, 1657-1660.

Li, X., Rohrer, F., Hofzumahaus, A., Brauers, T., Häseler, R., Bohn, B., Broch, S., Fuchs, H., Gomm, S., Holland, F., 2015. Response to Comment on "Missing gas-phase source of HONO inferred from Zeppelin measurements in the troposphere". Science 348, 1326-1326.

Li, X., Rohrer, F., Hofzumahaus, A., Brauers, T., Haseler, R., Bohn, B., Broch, S., Fuchs, H., Gomm, S., Holland, F., Jager, J., Kaiser, J., Keutsch, F.N., Lohse, I., Lu, K., Tillmann, R., Wegener, R., Wolfe, G.M., Mentel, T.F., Kiendler-Scharr, A., Wahner, A., 2014. Missing gas-phase source of HONO inferred from Zeppelin measurements in the troposphere. Science 344, 292-296.

Li, Y., An, J.L., Min, M., Zhang, W., Wang, F., Xie, P.H., 2011. Impacts of HONO sources on the air quality in Beijing, Tianjin and Hebei Province of China. Atmospheric Environment 45, 4735-4744.

Liao, S., Zhang, J., Yu, F., Zhu, M., Liu, J., Ou, J., Dong, H., Sha, Q., Zhong, Z., Xie, Y., Luo, H., Zhang, L., Zheng, J., 2021. High Gaseous Nitrous Acid (HONO) Emissions from Light-Duty Diesel Vehicles. Environmental science & technology 55, 200-208.

Lin, Y.L., Farley, R.D., Orville, H.D., 1983. Bulk Parameterization of the Snow Field in a Cloud Model. J Clim Appl Meteorol 22, 1065-1092.

Liu, J., Li, S., Zeng, J., Mekic, M., Yu, Z., Zhou, W., Loisel, G., Gandolfo, A., Song, W., Wang, X., Zhou, Z., Herrmann, H., Li, X., Gligorovski, S., 2019. Assessing indoor gas phase oxidation capacity through real-time measurements of HONO and NO_x in Guangzhou, China. Environ Sci Process Impacts 21, 1393-1402.

Liu, Y., Zhang, Y., Lian, C., Yan, C., Feng, Z., Zheng, F., Fan, X., Chen, Y., Wang, W., Chu, B., Wang, Y., Cai, J., Du, W., Daellenbach, K.R., Kangasluoma, J., Bianchi, F., Kujansuu, J., Petäjä, T., Wang, X., Hu, B., Wang, Y., Ge, M., He, H., Kulmala, M., 2020. The promotion effect of nitrous acid on aerosol formation in wintertime in Beijing: the possible contribution of traffic-related emissions. Atmospheric Chemistry and Physics 20, 13023-13040.

Liu, Z., Wang, Y., Costabile, F., Amoroso, A., Zhao, C., Huey, L.G., Stickel, R., Liao, J., Zhu, T., 2014. Evidence of aerosols as a media for rapid daytime HONO production over China. Environmental Science & Technology 48, 14386-14391.

Lu, X., Zhang, L., Wang, X.L., Gao, M., Li, K., Zhang, Y.Z., Yue, X., Zhang, Y.H., 2020. Rapid Increases in Warm-Season Surface Ozone and Resulting Health Impact in China Since 2013. Environmental Science & Technology Letters 7, 240-247.

Ma, J., Liu, Y., Han, C., Ma, Q., Liu, C., He, H., 2013. Review of heterogeneous photochemical reactions of NO_y on aerosol — A possible daytime source of nitrous acid (HONO) in the atmosphere. Journal of Environmental Sciences 25, 326-334.

Ma, Z.Q., Xu, J., Quan, W.J., Zhang, Z.Y., Lin, W.L., Xu, X.B., 2016. Significant increase of surface ozone at a rural site, north of eastern China. Atmospheric Chemistry and Physics 16, 3969-3977.

Maji, K.J., Namdeo, A., 2021. Continuous increases of surface ozone and associated premature mortality growth in China during 2015-2019. Environ Pollut 269, 116183.

Marion, A., Morin, J., Gandolfo, A., Ormeno, E., D'Anna, B., Wortham, H., 2021. Nitrous acid formation on Zea mays leaves by heterogeneous reaction of nitrogen dioxide in the laboratory. Environ Res 193, 110543.

Meng, F.H., Qin, M., Tang, K., Duan, J., Fang, W., Liang, S.X., Ye, K.D., Xie, P.H., Sun, Y.L., Xie, C.H., Ye, C.X., Fu, P.Q., Liu, J.G., Liu, W.Q., 2020. High-resolution vertical distribution and sources of HONO and NO_2 in the nocturnal boundary layer in urban Beijing, China. Atmospheric Chemistry and Physics 20, 5071-5092.

Mills, G., Buse, A., Gimeno, B., Bermejo, V., Holland, M., Emberson, L., Pleijel, H., 2007. A synthesis of AOT40-based response functions and critical levels of ozone for agricultural and horticultural crops. Atmospheric Environment 41, 2630-2643.

Mills, G., Sharps, K., Simpson, D., Pleijel, H., Broberg, M., Uddling, J., Jaramillo, F., Davies, W.J., Dentener, F., Van den Berg, M., Agrawal, M., Agrawal, S.B., Ainsworth, E.A., Buker, P., Emberson, L., Feng, Z., Harmens, H., Hayes, F., Kobayashi, K., Paoletti, E., Van Dingenen, R., 2018. Ozone pollution will compromise efforts to increase global wheat production. Glob Chang Biol 24, 3560-3574.

Oswald, R., Behrendt, T., Ermel, M., Wu, D., Su, H., Cheng, Y., Breuninger, C., Moravek, A., Mougin, E., Delon, C., Loubet, B., Pommerening-Roser, A., Sorgel, M., Poschl, U., Hoffmann, T., Andreae, M.O., Meixner, F.X., Trebs, I., 2013. HONO emissions from soil bacteria as a major source of atmospheric reactive nitrogen. Science 341, 1233-1235.

Pagsberg, P., Bjergbakke, E., Ratajczak, E., Sillesen, A., 1997. Kinetics of the gas phase reaction OH+NO (+M)->HONO (+M) and the determination of the UV absorption cross sections of HONO. Chemical Physics Letters 272, 383-390.

Perner, D., Platt, U., 1979. Detection of nitrous acid in the atmospeere by differential optical absorption. Geophysical Research Letters 6, 917-920.

Pitts, J.N., Wallington, T.J., Biermann, H.W., Winer, A.M., 1985. Identification and Measurement of Nitrous-Acid in an Indoor Environment. Atmospheric Environment 19, 763-767.

Qu, Y., Chen, Y., Liu, X., Zhang, J., Guo, Y., An, J., 2019. Seasonal effects of additional HONO sources and the heterogeneous reactions of N_2O_5 on nitrate in the North China Plain. The Science of the total environment 690, 97-107.

Reed, C., Evans, M.J., Crilley, L.R., Bloss, W.J., Sherwen, T., Read, K.A., Lee, J.D., Carpenter, L.J., 2017. Evidence for renoxification in the tropical marine boundary layer. Atmospheric Chemistry and Physics 17, 4081-4092.

Richards, B.L., Middleton, J.T., Hewitt, W.B., 1958. Air Pollution With Relation to Agronomic Crops: V. Oxidant Stipple of Grape. Agronomy Journal 50, 559-561.

Rohrer, F., Bohn, B., Brauers, T., Bruning, D., Johnen, F.J., Wahner, A., Kleffmann, J., 2005. Characterisation of the photolytic HONO-source in the atmosphere simulation chamber SAPHIR. Atmospheric Chemistry and Physics 5, 2189-2201.

Romer, P.S., Wooldridge, P.J., Crounse, J.D., Kim, M.J., Wennberg, P.O., Dibb, J.E., Scheuer, E., Blake, D.R., Meinardi, S., Brosius, A.L., Thames, A.B., Miller, D.O., Brune, W.H., Hall, S.R., Ryerson, T.B., Cohen, R.C., 2018. Constraints on Aerosol Nitrate Photolysis as a Potential Source of HONO and NO_x. Environmental Science & Technology 52, 13738-13746.

Rondon, A., Sanhueza, E., 1989. High HONO atmospheric concentrations during vegetation burning in the tropical savannah. Tellus Ser. B-Chem. Phys. Meteorol. 41, 474-477.

Ryan, R.G., Rhodes, S., Tully, M., Wilson, S., Jones, N., Friess, U., Schofield, R., 2018. Daytime HONO, NO_2 and aerosol distributions from MAX-DOAS observations in Melbourne. Atmospheric Chemistry and Physics 18, 13969-13985.

Saliba, N.A., Mochida, M., Finlayson-Pitts, B.J., 2000. Laboratory studies of sources of HONO in polluted urban atmospheres. Geophysical Research Letters 27, 3229-3232.

Sakamaki, F., Hatakeyama, S., Akimoto, H., 1983. Formation of Nitrous-Acid and Nitric-Oxide in the Heterogeneous Dark Reaction of Nitrogen-Dioxide and Water-Vapor in a Smog Chamber. International Journal of Chemical Kinetics 15, 1013-1029.

Sarwar, G., Roselle, S.J., Mathur, R., Appel, W., Dennis, R.L., Vogel, B., 2008. A comparison of CMAQ HONO predictions with observations from the northeast oxidant and particle study. Atmospheric Environment 42, 5760-5770.

Selin, N.E., Wu, S., Nam, K.M., Reilly, J.M., Paltsev, S., Prinn, R.G., Webster, M.D., 2009. Global health and economic impacts of future ozone pollution. Environmental Research Letters 4, 044014.

Shi, Q., Tao, Y., Krechmer, J.E., Heald, C.L., Murphy, J.G., Kroll, J.H., Ye, Q., 2021. Laboratory Investigation of Renoxification from the Photolysis of Inorganic Particulate Nitrate. Environmental science & technology, 55, 854−861.

Shi, X., Ge, Y., Zheng, J., Ma, Y., Ren, X., Zhang, Y., 2020. Budget of nitrous acid and its impacts on atmospheric oxidative capacity at an urban site in the central Yangtze River Delta region of China. Atmospheric Environment 238, 117725.

Sillman, S., 1995. The use of NO_y, H_2O_2, and HNO_3 as indicators for ozone-NO_x-hydrocarbon sensitivity in urban locations. Journal of Geophysical Research: Atmospheres 100, 14175-14188.

Slater, E.J., Whalley, L.K., Woodward-Massey, R., Ye, C.X., Lee, J.D., Squires, F., Hopkins, J.R., Dunmore, R.E., Shaw, M., Hamilton, J.F., Lewis, A.C., Crilley, L.R., Kramer, L., Bloss, W., Vu, T., Sun, Y.L., Xu, W.Q., Yue, S.Y., Ren, L.J., Acton, W.J.F., Hewitt, C.N., Wang, X.M., Fu, P.Q., Heard, D.E., 2020. Elevated levels of OH observed in haze events during wintertime in central Beijing. Atmospheric Chemistry and Physics 20, 14847-14871.

Sorgel, M., Trebs, I., Serafimovich, A., Moravek, A., Held, A., Zetzsch, C., 2011. Simultaneous HONO measurements in and above a forest canopy: influence of turbulent exchange on mixing ratio differences. Atmospheric Chemistry and Physics 11, 841-855.

Stuhl, F., Niki, H., 1972. Flash Photochemical Study of the Reaction OH+NO+M Using Resonance Fluorescent Detection of OH. The Journal of Chemical Physics 57, 3677-3679.

Tan, Z.F., Rohrer, F., Lu, K.D., Ma, X.F., Bohn, B., Broch, S., Dong, H.B., Fuchs, H., Gkatzelis, G.I., Hofzumahaus, A., Holland, F., Li, X., Liu, Y., Liu, Y.H., Novelli, A., Shao, M., Wang, H.C., Wu, Y.S., Zeng, L.M., Hu, M., Kiendler-Scharr, A., Wahner, A., Zhang, Y.H., 2018. Wintertime

photochemistry in Beijing: observations of RO_x radical concentrations in the North China Plain during the BEST-ONE campaign. Atmospheric Chemistry and Physics 18, 12391-12411.

Tang, M.J., Huang, X., Lu, K.D., Ge, M.F., Li, Y.J., Cheng, P., Zhu, T., Ding, A.J., Zhang, Y.H., Gligorovski, S., Song, W., Ding, X., Bi, X.H., Wang, X.M., 2017. Heterogeneous reactions of mineral dust aerosol: implications for tropospheric oxidation capacity. Atmospheric Chemistry and Physics 17, 11727-11777.

Tang, Y., An, J., Wang, F., Li, Y., Qu, Y., Chen, Y., Lin, J., 2015. Impacts of an unknown daytime HONO source on the mixing ratio and budget of HONO, and hydroxyl, hydroperoxyl, and organic peroxy radicals, in the coastal regions of China. Atmospheric Chemistry and Physics 15, 9381-9398.

Theys, N., Volkamer, R., Mueller, J.F., Zarzana, K.J., Kille, N., Clarisse, L., De Smedt, I., Lerot, C., Finkenzeller, H., Hendrick, F., Koenig, T.K., Lee, C.F., Knote, C., Yu, H., Van Roozendael, M., 2020. Global nitrous acid emissions and levels of regional oxidants enhanced by wildfires. Nature Geoscience 13, 681-686.

Tie, X., Long, X., Li, G., Zhao, S., Cao, J., Xu, J., 2019. Ozone enhancement due to the photodissociation of nitrous acid in eastern China. Atmospheric Chemistry and Physics 19, 11267-11278.

VandenBoer, T.C., Brown, S.S., Murphy, J.G., Keene, W.C., Young, C.J., Pszenny, A.A.P., Kim, S., Warneke, C., de Gouw, J.A., Maben, J.R., Wagner, N.L., Riedel, T.P., Thornton, J.A., Wolfe, D.E., Dube, W.P., Ozturk, F., Brock, C.A., Grossberg, N., Lefer, B., Lerner, B., Middlebrook, A.M., Roberts, J.M., 2013. Understanding the role of the ground surface in HONO vertical structure: High resolution vertical profiles during NACHTT-11. J Geophys Res-Atmos 118, 10155-10171.

Villena, G., Kleffmann, J., Kurtenbach, R., Wiesen, P., Lissi, E., Rubio, M.A., Croxatto, G., Rappenglück, B., 2011. Vertical gradients of HONO, NO_x and O_3 in Santiago de Chile. Atmospheric Environment 45, 3867-3873.

Wang, F., An, J.L., Li, Y., Tang, Y.J., Lin, J., Qu, Y., Chen, Y., Zhang, B., Zhai, J., 2014. Impacts of uncertainty in AVOC emissions on the summer RO_x budget and ozone production rate in the three most rapidly-developing economic growth regions of China. Advances in Atmospheric Sciences 31, 1331-1342.

Wang, X., Zhang, Y., Hu, Y., Zhou, W., Lu, K., Zhong, L., Zeng, L., Shao, M., Hu, M., Russell, A.G., 2010. Process analysis and sensitivity study of regional ozone formation over the Pearl River Delta, China, during the PRIDE-PRD2004 campaign using the Community Multiscale Air Quality modeling system. Atmospheric Chemistry and Physics 10, 4423-4437.

Wang, Y., Apituley, A., Bais, A., Beirle, S., Benavent, N., Borovski, A., Bruchkouski, I., Chan, K.L., Donner, S., Drosoglou, T., Finkenzeller, H., Friedrich, M.M., Friess, U., Garcia-Nieto, D., Gomez-Martin, L., Hendrick, F., Hilboll, A., Jin, J.L., Johnston, P., Koenig, T.K., Kreher, K., Kumar, V., Kyuberis, A., Lampel, J., Liu, C., Liu, H.R., Ma, J.Z., Polyansky, O.L., Postylyakov, O., Querel, R., Saiz-Lopez, A., Schmitt, S., Tian, X., Tirpitz, J.L., Van Roozendael, M., Volkamer, R., Wang, Z.R., Xie, P.H., Xing, C.Z., Xu, J., Yela, M., Zhang, C.X., Wagner, T., 2020. Inter-comparison of MAX-DOAS measurements of tropospheric HONO slant column densities and vertical profiles during the CINDI-2 campaign. Atmospheric Measurement Techniques 13, 5087-5116.

Wang, Y., Dörner, S., Donner, S., Böhnke, S., De Smedt, I., Dickerson, R.R., Dong, Z., He, H., Li, Z., Li, Z., Li, D., Liu, D., Ren, X., Theys, N., Wang, Y., Wang, Y., Wang, Z., Xu, H., Xu, J., Wagner,

T., 2019. Vertical profiles of NO_2, SO_2, HONO, HCHO, CHOCHO and aerosols derived from MAX-DOAS measurements at a rural site in the central western North China Plain and their relation to emission sources and effects of regional transport. Atmospheric Chemistry and Physics 19, 5417-5449.

Wilkinson, S., Mills, G., Illidge, R., Davies, W.J., 2012. How is ozone pollution reducing our food supply? J Exp Bot 63, 527-536.

Wong, K.W., Oh, H.J., Lefer, B.L., Rappengluck, B., Stutz, J., 2011. Vertical profiles of nitrous acid in the nocturnal urban atmosphere of Houston, TX. Atmospheric Chemistry and Physics 11, 3595-3609.

Wong, K.W., Tsai, C., Lefer, B., Haman, C., Grossberg, N., Brune, W.H., Ren, X., Luke, W., Stutz, J., 2012. Daytime HONO vertical gradients during SHARP 2009 in Houston, TX. Atmospheric Chemistry and Physics 12, 635-652.

Wu, D., Horn, M.A., Behrendt, T., Muller, S., Li, J., Cole, J.A., Xie, B., Ju, X., Li, G., Ermel, M., Oswald, R., Frohlich-Nowoisky, J., Hoor, P., Hu, C., Liu, M., Andreae, M.O., Poschl, U., Cheng, Y., Su, H., Trebs, I., Weber, B., Sorgel, M., 2019. Soil HONO emissions at high moisture content are driven by microbial nitrate reduction to nitrite: tackling the HONO puzzle. ISME J 13, 1688-1699.

Xing, C., Liu, C., Hu, Q., Fu, Q., Wang, S., Lin, H., Zhu, Y., Wang, S., Wang, W., Javed, Z., 2021. Vertical distributions of wintertime atmospheric nitrogenous compounds and the corresponding OH radicals production in Leshan, southwest China. Journal of Environmental Sciences 105, 44-55.

Xing, L., Wu, J.R., Elser, M., Tong, S.R., Liu, S.X., Li, X., Liu, L., Cao, J.J., Zhou, J.M., El-Haddad, I., Huang, R.J., Ge, M.F., Tie, X.X., Prevot, A.S.H., Li, G.H., 2019. Wintertime secondary organic aerosol formation in Beijing-Tianjin-Hebei (BTH): contributions of HONO sources and heterogeneous reactions. Atmospheric Chemistry and Physics 19, 2343-2359.

Xu, J., Zhang, Y.H., Wang, W., 2006. Numerical study on the impacts of heterogeneous reactions on ozone formation in the Beijing urban area. Advances in Atmospheric Sciences 23, 605-614.

Xu, W., Yang, W., Han, C., Yang, H., Xue, X., 2021. Significant influences of TiO_2 crystal structures on NO_2 and HONO emissions from the nitrates photolysis. Journal of Environmental Sciences 102, 198-206.

Xue, C., Zhang, C., Ye, C., Liu, P., Catoire, V., Krysztofiak, G., Chen, H., Ren, Y., Zhao, X., Wang, J., Zhang, F., Zhang, C., Zhang, J., An, J., Wang, T., Chen, J., Kleffmann, J., Mellouki, A., Mu, Y., 2020. HONO Budget and Its Role in Nitrate Formation in the Rural North China Plain. Environmental Science & Technology 54, 11048-11057.

Xue, C.Y., Ye, C., Zhang, C.L., Catoire, V., Liu, P.F., Gu, R.R., Zhang, J.W., Ma, Z.B., Zhao, X.X., Zhang, W.Q., Ren, Y.G., Krysztofiak, G., Tong, S.R., Xue, L.K., An, J.L., Ge, M.F., Mellouki, A., Mu, Y.J., 2021. Evidence for Strong HONO Emission from Fertilized Agricultural Fields and its Remarkable Impact on Regional O_3 Pollution in the Summer North China Plain. ACS Earth Space Chem. 5, 340-347.

Yang, K., Kong, L., Tong, S., Shen, J., Chen, L., Jin, S., Wang, C., Sha, F., Wang, L., 2021a. Double High-Level Ozone and $PM_{2.5}$ Co-Pollution Episodes in Shanghai, China: Pollution Characteristics and Significant Role of Daytime HONO. Atmosphere 12, 557.

Yang, W., Han, C., Yang, H., Xue, X., 2018. Significant HONO formation by the photolysis of nitrates in the presence of humic acids. Environ Pollut 243, 679-686.

Yang, W., Han, C., Zhang, T., Tang, N., Yang, H., Xue, X., 2021b. Heterogeneous photochemical uptake of NO_2 on the soil surface as an important ground-level HONO source. Environ. Pollut. 271, 116289.

Ye, C., Gao, H., Zhang, N., Zhou, X., 2016a. Photolysis of Nitric Acid and Nitrate on Natural and Artificial Surfaces. Environmental Science & Technology 50, 3530-3536.

Ye, C., Zhang, N., Gao, H., Zhou, X., 2017. Photolysis of Particulate Nitrate as a Source of HONO and NO_x. Environmental Science & Technology 51, 6849-6856.

Ye, C., Zhou, X., Pu, D., Stutz, J., Festa, J., Spolaor, M., Cantrell, C., Mauldin, R.L., Weinheimer, A., Haggerty, J., 2015. Comment on "Missing gas-phase source of HONO inferred from Zeppelin measurements in the troposphere". Science 348, 1326-d.

Ye, C., Zhou, X., Pu, D., Stutz, J., Festa, J., Spolaor, M., Tsai, C., Cantrell, C., Mauldin, R.L., 3rd, Campos, T., Weinheimer, A., Hornbrook, R.S., Apel, E.C., Guenther, A., Kaser, L., Yuan, B., Karl, T., Haggerty, J., Hall, S., Ullmann, K., Smith, J.N., Ortega, J., Knote, C., 2016b. Rapid cycling of reactive nitrogen in the marine boundary layer. Nature 532, 489-491.

Zaveri, R.A., Easter, R.C., Fast, J.D., Peters, L.K., 2008. Model for Simulating Aerosol Interactions and Chemistry (MOSAIC). J Geophys Res-Atmos 113. doi:10.1029/2007JD008782.

Zhang, H.L., Li, J.Y., Ying, Q., Yu, J.Z., Wu, D., Cheng, Y., He, K.B., Jiang, J.K., 2012. Source apportionment of $PM_{2.5}$ nitrate and sulfate in China using a source-oriented chemical transport model. Atmospheric Environment 62, 228-242.

Zhang, J., An, J., Qu, Y., Liu, X., Chen, Y., 2019a. Impacts of potential HONO sources on the concentrations of oxidants and secondary organic aerosols in the Beijing-Tianjin-Hebei region of China. The Science of the total environment 647, 836-852.

Zhang, J., Chen, J., Xue, C., Chen, H., Zhang, Q., Liu, X., Mu, Y., Guo, Y., Wang, D., Chen, Y., Li, J., Qu, Y., An, J., 2019b. Impacts of six potential HONO sources on HO_x budgets and SOA formation during a wintertime heavy haze period in the North China Plain. The Science of the total environment 681, 110-123.

Zhang, J., Guo, Y., Qu, Y., Chen, Y., Yu, R., Xue, C., Yang, R., Zhang, Q., Liu, X., Mu, Y., Wang, J., Ye, C., Zhao, H., Sun, Q., Wang, Z., An, J., 2020a. Effect of potential HONO sources on peroxyacetyl nitrate (PAN) formation in eastern China in winter. Journal of Environmental Sciences 94, 81-87.

Zhang, J., Ran, H., Guo, Y., Xue, C., Liu, X., Qu, Y., Sun, Y., Zhang, Q., Mu, Y., Chen, Y., Wang, J., An, J., 2022. High crop yield losses induced by potential HONO sources — A modelling study in the North China Plain. Science of The Total Environment 803, 149929.

Zhang, L., Wang, T., Zhang, Q., Zheng, J.Y., Xu, Z., Lv, M.Y., 2016. Potential sources of nitrous acid (HONO) and their impacts on ozone: A WRF-Chem study in a polluted subtropical region. J Geophys Res-Atmos 121, 3645-3662.

Zhang, N., Zhou, X.L., Shepson, P.B., Gao, H.L., Alaghmand, M., Stirm, B., 2009. Aircraft measurement of HONO vertical profiles over a forested region. Geophysical Research Letters 36. doi:10.1029/2009GL038999.

Zhang, Q., Geng, G., 2019. Impact of clean air action on $PM_{2.5}$ pollution in China. Science China Earth Sciences 62, 1845-1846.

Zhang, S., Sarwar, G., Xing, J., Chu, B., Xue, C., Sarav, A., Ding, D., Zheng, H., Mu, Y., Duan, F., Ma, T., He, H., 2021. Improving the representation of HONO chemistry in CMAQ and examining its impact on haze over China. Atmospheric Chemistry and Physics 21, 15809-15826.

Zhang, W., Tong, S., Ge, M., An, J., Shi, Z., Hou, S., Xia, K., Qu, Y., Zhang, H., Chu, B., Sun, Y., He,

H., 2019c. Variations and sources of nitrous acid (HONO) during a severe pollution episode in Beijing in winter 2016. The Science of the total environment 648, 253-262.

Zhang, W.Q., Tong, S.R., Jia, C.H., Wang, L.L., Liu, B.X., Tang, G.Q., Ji, D.S., Hu, B., Liu, Z.R., Li, W.R., Wang, Z., Liu, Y., Wang, Y.S., Ge, M.F., 2020b. Different HONO Sources for Three Layers at the Urban Area of Beijing. Environmental science & technology 54, 12870-12880.

Zhao, H., Zhang, Y., Qi, Q., Zhang, H., 2021. Evaluating the Impacts of Ground-Level O_3 on Crops in China. Current Pollution Reports 7, 565-578.

Zheng, H., Song, S., Sarwar, G., Gen, M., Wang, S., Ding, D., Chang, X., Zhang, S., Xing, J., Sun, Y., Ji, D., Chan, C.K., Gao, J., McElroy, M.B., 2020. Contribution of Particulate Nitrate Photolysis to Heterogeneous Sulfate Formation for Winter Haze in China. Environmental Science & Technology Letters 7, 632-638.

Zhou, X., Gao, H., He, Y., Huang, G., Bertman, S.B., Civerolo, K., Schwab, J., 2003. Nitric acid photolysis on surfaces in low-NO_x environments: Significant atmospheric implications. Geophysical Research Letters 30. doi:10.1029/2003GL018620.

Zhu, C., Xiang, B., Zhu, L., Cole, R., 2008. Determination of absorption cross sections of surface-adsorbed HNO_3 in the 290–330 nm region by Brewster angle cavity ring-down spectroscopy. Chemical Physics Letters 458, 373-377.

Zhu, Y.W., Liu, W.Q., Fang, J., Xie, P.H., Dou, K., Qin, M., Si, F.Q., 2011. Monitoring and Analysis of Vertical Profile of Atmospheric HONO, NO_2 in Boundary Layer of Beijing. Spectroscopy and Spectral Analysis 31, 1078-1082.